A COMPARATIVE STUDY OF ANISOTROPIC HYPERELASTIC MODELS OF BIOLOGICAL SOFT TISSUES

A THESIS SUBMITTED TO
THE GRADUATE SCHOOL OF NATURAL AND APPLIED SCIENCES
OF
MIDDLE EAST TECHNICAL UNIVERSITY

BY

ALP KAĞAN AÇAN

IN PARTIAL FULFILLMENT OF THE REQUIREMENTS
FOR
THE DEGREE OF MASTER OF SCIENCE
IN
MECHANICAL ENGINEERING

AUGUST 2021

Approval of the thesis:

A COMPARATIVE STUDY OF ANISOTROPIC HYPERELASTIC MODELS OF BIOLOGICAL SOFT TISSUES

submitted by **ALP KAĞAN AÇAN** in partial fulfillment of the requirements for the degree of **Master of Science in Mechanical Engineering Department, Middle East Technical University** by,

Prof. Dr. Halil Kalıpçılar
Dean, Graduate School of **Natural and Applied Sciences** _____

Prof. Dr. Mehmet Ali Sahir Arıkan
Head of Department, **Mechanical Engineering** _____

Assoc. Prof. Dr. Hüsnü Dal
Supervisor, **Mechanical Engineering, METU** _____

Examining Committee Members:

Prof. Dr. Suat Kadıoğlu
Mechanical Engineering, METU _____

Assoc. Prof. Dr. Hüsnü Dal
Mechanical Engineering, METU _____

Assoc. Prof. Dr. Sezer Özerinç
Mechanical Engineering, METU _____

Assoc. Prof. Dr. Ercan Gürses
Aerospace Engineering, METU _____

Assist. Prof. Dr. Omer Music
Mechanical Engineering, TED University _____

Date : 23.08.2021

I hereby declare that all information in this document has been obtained and presented in accordance with academic rules and ethical conduct. I also declare that, as required by these rules and conduct, I have fully cited and referenced all material and results that are not original to this work.

Name, Surname: Alp Kağan Açan

Signature :

ABSTRACT

A COMPARATIVE STUDY OF ANISOTROPIC HYPERELASTIC MODELS OF BIOLOGICAL SOFT TISSUES

Açan, Alp Kağan
M.S., Department of Mechanical Engineering
Supervisor: Assoc. Prof. Dr. Hüsnü Dal

August 2021, 82 pages

In the last two decades, there has been significant growth of interest in the mechanical behavior of biological soft tissues approached from the continuum mechanical perspective. A plenty of constitutive models have been proposed that represent the anisotropic hyperelastic behavior of biological soft tissues. Generally, invariant and fiber dispersion-based models are two main categories considered during the modeling steps. Among the anisotropic models, fiber dispersion-based constitutive models are known to have high performance for capturing the anisotropic behavior of tissues over invariant-based models. The type of the biological soft tissues and the number of available experimental data set under different loading cases play an important role in choosing the appropriate model. With the increasing number of hyperelastic models, a comparison among the models and choosing a proper one becomes a crucial factor for researchers in the field. In this study, the fitting performance of 9 anisotropic hyperelastic models has been investigated for three different tissues, abdominal aortic aneurysm tissue, linea alba, and rectus sheath. In order to obtain the parameters of each constitutive model, a genetic algorithm has been utilized. Further improvement of the results is achieved through the fmincon utility of MATLAB. Equibiaxial dataset

for abdominal aortic aneurysm tissue, uniaxial dataset for linea alba, and uniaxial tension dataset for rectus sheath have been considered during parameter optimization.

Keywords: hyperelasticity, soft tissue, fiber dispersion, parameter optimization

ÖZ

BİYOLOJİK YUMUŞAK DOKULARIN ANİZOTROPİK HİPERELASTİK YAPISAL MODELLERİNİN KARŞILAŞTIRMALI BİR ÇALIŞMASI

Açan, Alp Kağan
Yüksek Lisans, Makina Mühendisliği Bölümü
Tez Yöneticisi: Doç. Dr. Hüsnü Dal

Ağustos 2021 , 82 sayfa

Son yirmi yılda, biyolojik yumuşak dokuların mekanik davranışına süreklilik mekanik perspektifinden yaklaşılan ilgide önemli bir artış olmuştur. Birçok araştırmacı, biyolojik yumuşak dokuların anizotropik hiperelastik davranışını temsil etmek için çeşitli yapısal modeller geliştirmiştir. Genel olarak, değişmez ve fiber dağılımına dayalı modeller, modelleme adımları sırasında dikkate alınan iki ana kategoridir. Anizotropik modeller arasında, fiber dağılımına dayalı yapısal modellerin, değişmez tabanlı modellere göre dokuların anizotropik davranışını yakalamak için yüksek performansa sahip olduğu bilinmektedir. Biyolojik yumuşak dokuların tipi ve farklı yükleme durumları altında mevcut deneysel veri setlerinin sayısı, uygun modelin seçilmesinde önemli bir rol oynamaktadır. Hiperelastik modellerin sayısının artması ile modeller arasında karşılaştırma yapmak ve uygun olanı seçmek bu alandaki araştırmacılar için çok önemli bir faktör haline gelmektedir. Bu çalışmada 9 anizotropik hiperelastik modelin uyum performansı sunulmuştur. Yapısal modellerin parametreleri, genetik bir algoritma kullanılarak bulunmuştur. MATLAB bünyesindeki fmincon yardımcı programı kullanılarak sonuçların daha da iyileştirilmesi gerçekleştirilmiştir. Parametre op-

timizasyonu sırasında tek eksenli ve eş-çift eksenli yükleme modları için iyi bilinen veri setleri göz önünde bulundurulmuştur.

Anahtar Kelimeler: hiperelastisite, yumuşak doku, lif dağılımı, parametre optimizasyonu

To my family

ACKNOWLEDGMENTS

First of all, I would like to express my deepest thanks to my advisor Assoc. Prof. Dr. Hüsnü Dal for his support and guidance throughout my thesis study. I want to thank Ciara Durcan from Swansea University for supplying experimental data used in this thesis. I would also like to thank Kemal Açıkgöz for his suggestions and comments during my research. Last but not least, I would like to express my sincere gratitude to my parents Ali Açan and Dudu Açan, and my sister Eda Aybüke Açan.

TABLE OF CONTENTS

LIST OF TABLES

TABLES

LIST OF FIGURES

FIGURES

LIST OF ABBREVIATIONS

AAA	Abdominal Aortic Aneurysm
ET	Equibiaxial Tension
UT	Uniaxial Tension
AI	Angular Integration
GST	Generalized Structure Tensor
PDF	Probability Distribution Function
NOP	Number of Parameters
QOF	Quality of Fit
NY	Newman-Yin
HGO	Holzapfel-Gasser-Ogden
HSGR	Holzapfel-Sommer-Gasser-Regitnig
OS	Ogden-Saccomandi
DBB	Driessen-Bouten-Baaijens
GOH	Gasser-Ogden-Holzapfel
AMDM	Alastrué-Martinez-Doblaré-Menzel
ASMD	Alastrué-Saéz-Martinez-Doblaré
HNORS	Holzapfel-Niestrawska-Ogden-Reinisch-Schriefl

CHAPTER 1

INTRODUCTION

Biological tissues may be classified into two categories based on their histological nature - hard or soft. Bone or tooth has high mineral concentration and is considered as hard tissue. All other tissues can be considered soft tissues such as arterial walls, skin, muscles, and other organs. Soft tissues are composed of cells, of extracellular matrix. The cellular part of soft tissues includes fibrocytes cells which produce tissue protein fibers such as collagen, elastin [56]. Extracellular matrix consists of fibers of collagen, elastin, reticulum, and ground substance which is a hydrophilic gel [26]. Collagen fibers are the largest fibers in size and are more important for the aspect of mechanical modeling since collagen is the main structural element that provides strength and structural integrity to soft tissues. Tissues have different collagenous structures depending on their functions and integrities. Depending on the orientation of fibers, the mechanical behavior of the tissue varies.

For dense connective tissues whose primary function is carrying tension loads, such as tendons and ligaments, collagen fibers have parallel alignment with subjected load direction. In linea alba, for instance, the architecture of collagen fibers has variable formation, see Figure 1.1. For an arterial wall, the architecture of collagen fibers is much more complex. In the arterial wall, histological evidence shows that collagen fibers helically bind the outer and inner layer of the arterial wall, while they bind circumferentially the middle layer [8], see Figure 1.2. Increasing our understanding of the microstructure and mechanical behavior of soft tissues is crucial for developing medical engineering applications and assisting tissue engineering. There are important clinical problems that require an understanding of biomechanics. One of the common examples is the treatment of coronary artery disease. Only by developing accurate mechanical models, improved interventional devices (eg., intravascular

stents, balloon catheters used in angioplasty, atherectomy devices) can be designed. Assisting tissue engineering is also another purpose of studies on the mechanical behavior of soft tissues. With this understanding, in the last two decades, interest in constitutive modeling of soft tissues increased extensively. The various hyperelastic constitutive model was developed to represent mechanical behavior of soft tissue, see the review of Chagnon et al. [11].

Hyperelastic modeling is not enough to capture the time-dependent mechanical behavior of soft tissue. For instance, Cansız et al. [10] proposed an orthotropic viscoelastic material model for passive myocardium. In another study, Cansız et al. [9] described the active behavior of the myocardium using an electro-visco-elasticity model. Dal et al. [18] proposed a finite element algorithm for the bidomain-based approach to cardiac electromechanics. In the above examples, the soft tissue was modeled by the viscoelastic or electro-visco-elastic model. However, hyperelastic models were used as a ground model to represent the base elastic behavior of soft tissues.

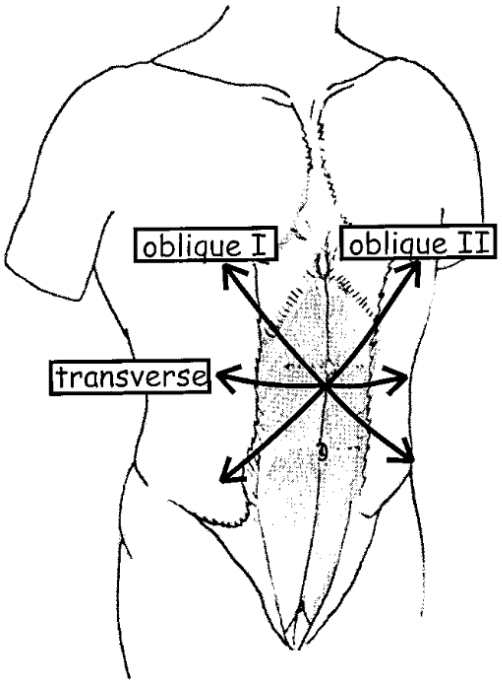

Figure 1.1: Main fiber directions of linea alba, adopted from [5].

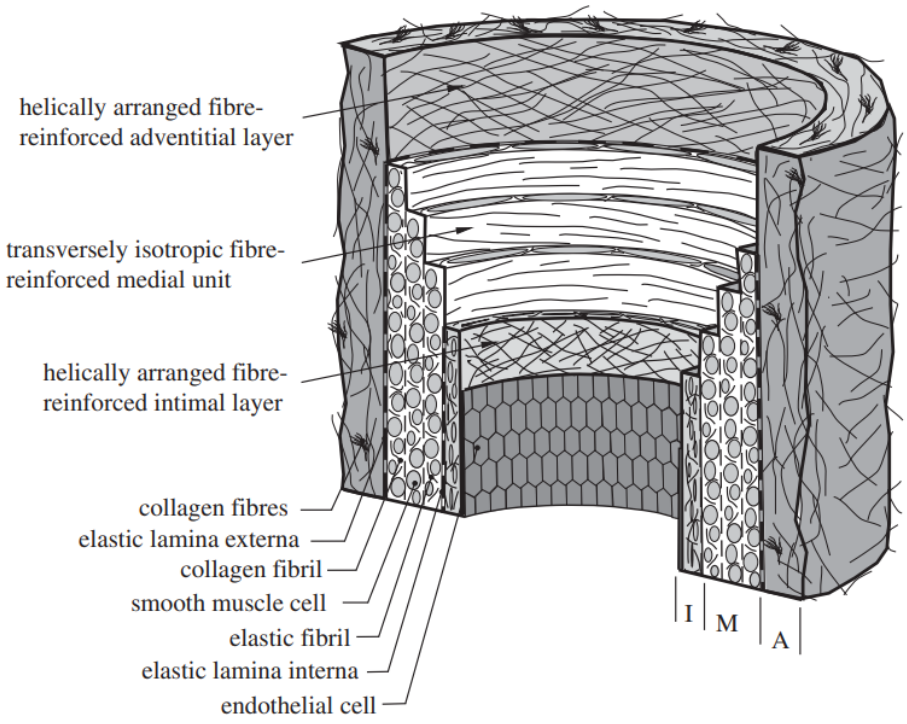

Figure 1.2: Idealized histological structure of human healthy artery. An arterial wall has 3 three layers: intima (I), media (M), adventitia (A); adopted from [28]

1.1 Mechanical behavior of soft tissues

Since the histological structures of each soft tissue are various, they have unique behavior, however, general characteristics are common to many tissues. Modeling biological soft tissues is challenging due to the anisotropic nature and highly non-linear mechanical behavior. Anisotropic behavior occurs since tissues are natural composite materials in which collagen, elastin, and reticular fibers are embedded into cells and extra-cellular ground substances. The ground substance mainly contains tissue fluids and water, therefore, soft tissues behave as a fully/quasi incompressible material. Unlike conventional composite materials, the fibers in soft tissues are presented in the wavy form in unloaded mode, they straighten when subjected to tension load. Thus, many researchers assume that collagen fibers do not support a compressive load, and they exclude fibers under compression [1, 3, 24, 35, 36, 55]. Typically, the non-linear tensile behavior of soft tissue has a J-shaped form, as shown in Figure 1.3. The mechanical behavior of soft tissues depends on time and dissipates energy, nevertheless,

the elastic behavior dominates and they show asymptotic behavior when dissipation goes to zero. For this reason, most of the tissue were discussed in the context of hyperelasticity [11].

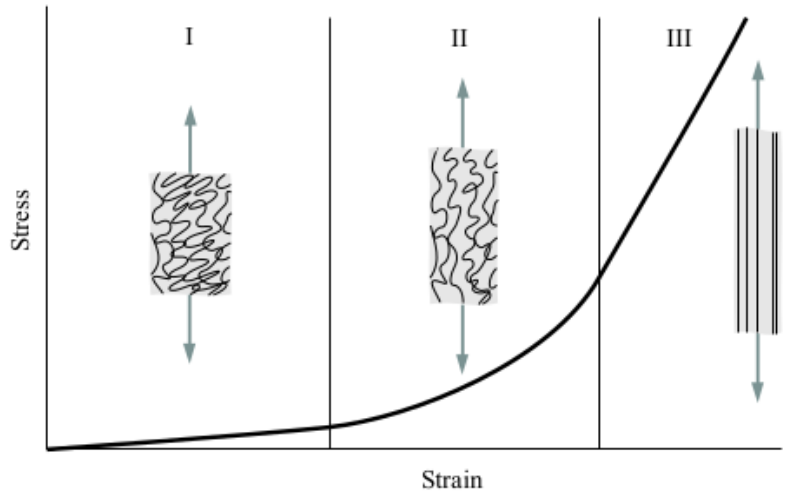

Figure 1.3: Typical non-linear tension behavior of soft tissue, adopted from [32]. In region I, fibers do not actively contibute to the mechanical response; in region II, fibers are straightened, and their contribution to mechanical response can be observed; in region III, fibers are fully straightened, and their mechanical contribution is the dominant factor.

1.2 Literature overview

1.2.1 Experimental studies

A variety of experimental loading modes can be used to characterise soft biological tissues. Amongst the most popular are uniaxial tension, biaxial tension and pure shear. This section outlines these test conditions in the context of tensile loading, and provides a collection of experimental results from literature which investigate the mechanical behaviour of soft tissues. The experimental proceedure for each different loading mode is explained and the final data is described.

Uniaxial tension, as the name suggests, is when elongation occurs in only one direction. Samples much greater in length than width, typically with a ratio of at least 4:1

(length : width), are stretched along the axis parallel to its length, as seen in Figure 2.4. The length to width ratio allows the assumption that tensile stresses within the sample other than those present along the axis of loading are zero. To experimentally investigate anisotropy, samples are usually cut and tested along both the $\boldsymbol{e}_1$- and $\boldsymbol{e}_2$-directions, as seen in Figure 2.4, with the assumption that no anisotropy derives from the $\boldsymbol{e}_3$-direction. As the reference axis can change depending on the samples being tested, all following discussion will take place in the context of the $\boldsymbol{e}_1$-direction samples, with the understanding that the same principles can be easily adapted by the reader for the $\boldsymbol{e}_2$-direction samples. Typically for uniaxial tension tests of metals or polymers, dogbone samples are employed to reduce the influence of end effects, and encourage fracture within the middle of the specimen and not at the grip location. However, for soft biological tissues, rectangular samples are often used instead due to the soft and delicate nature of the material making the punching of precise dogbone samples very difficult. The first study selected to present uniaxial tension data on soft biological tissues was by Cooney et al. [14], who investigated the uniaxial and equibiaxial tensile behaviour of the human linea alba. Cooney et al. [14] obtained 13 freshly frozen human cadaveric abdominal walls for their study and from these extracted the linea alba for their experiments. The linea alba is a collagenous part of the ventral abdominal wall whose collagen fibres are known to be anisotropically arranged. Prior to sample extraction, the human cadaveric abdominal walls were allowed to defrost for 36 hours at 4°C. The linea alba were then extracted from each abdominal wall and stored in phosphate-buffered saline solution until testing. For the uniaxial tension tests, 14 rectangular samples in total were obtained from 7 of the linea alba specimens. Seven samples were cut in both the longitudinal and transverse directions, with longitudinal and transverse referring to their respective anatomical axes. The length to width ratio of the rectangular samples was as close to the unaxial test condition as possible for the size of available tissue, with this equalling approximately 2:1 (length : width) for both directions. Prior to testing, samples were mounted in grips lined with emery paper to reduce any slippage during loading. The grips were tightened using a 0.2 Nm torque wrench to prevent over-tightening of the grips damaging the tissue. Six black dots were applied to the surface of the samples, as seen in Figure 1.4, before securing the samples in the modular mechanical testing machine seen in Figure 1.4a which was fitted with a 300 N load cell. During testing, a high definition

camera was used to collect images at a rate of 2 Hz. The post-processing of these images allowed for the calculation of sample strains by analysing the deformation of each black dot throughout stretching. A pre-stress of 0.1MPa was applied to all samples to remove any slack present. The tests were conducted at a quasi-static strain rate of 28.5% min^{-1}, and were stopped when either the load was greater than 90 N or if tearing had started to occur at the grips or along the length of the sample.

The transverse direction was found to be much stiffer than the longitudinal direction,

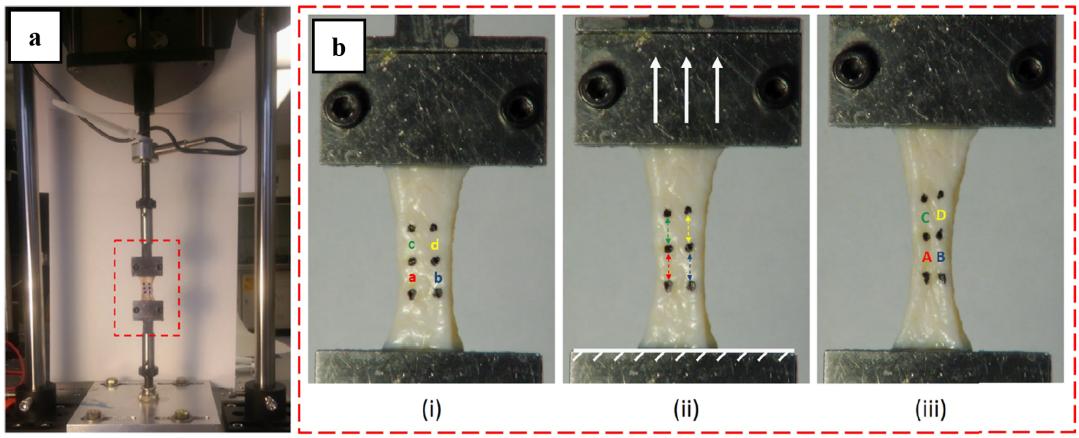

Figure 1.4: The experimental setup of the uniaxial testing machine (**a**) and close ups of a transverse sample undering various stages of tension (**b**) including before loading (i), during loading (ii) and at maximum stretch of the test, modified from Cooney et al. [14].

displaying the anisotropy of the tissue. Cooney et al. [14] found the slope of the most linear section of the curve to be approximately 72 MPa in the transverse direction and 8 MPa in the longitudinal direction.

The second study selected was uniaxial tension data by Martins et al. [50], who investigated uniaxial tensile behavior of human anterior rectus sheath. Martins et al. harvested the tissue samples from 12 fresh female cadavers. 6 rectangular samples were cut along both the direction of fibers and transverse to the direction of fibers. The thickness of samples was 1.00 mm with a 1:4 length to width ratio. The tests were conducted at a rate of 5 mm/min at room temperature. The tensile behavior was observed to be nonlinear in both the fiber direction and transverse to the fiber direction. Equibiaxial tension is defined as equal and simultaneous elongation along two orthogonal directions. It is used in the characterisation of soft biological tissues as it

is often considered to be more representative of the stresses experienced in vivo [14]. Square samples are used for the tests and the samples are equally loaded under tension on all four sides, as seen in Figure 2.4c. Due to this, the principal stretch in the $\boldsymbol{e}_1$- and $\boldsymbol{e}_2$-directions is equal to the experimental stretch, i.e. $\lambda_1 = \lambda_2 = \lambda$, leaving the $\boldsymbol{e}_3$-direction the only one unconstrained. If the material is considered incompressible, and due to the assumption of symmetry, $\lambda_3 = \lambda^{-2}$. The equibiaxial tension study selected was an investigation by Niestrawska et al. [52] on human abdominal aortas. They conducted equibiaxial tension experiments on both healthy and aneurysmatic abdominal aortas. The data used here was extracted from the experimental results on the abdominal aortic aneurysms which were obtained through surgical procedures conducted at the Department of Vascular Surgery, Medical University Graz, Austria. Aneurysms are defined as irreversible, localised dilatation of a vessel, which can in some cases lead to complete wall rupture. Eleven wall samples in total were collected from open aneurysm repair at the anterior side. The samples were stored at 4°C in Dublecco's modified Eagle's medium prior to testing. To prepare for testing, 20 $\times$ 20 mm patches were cut from the aneurysmatic abdominal aorta walls. Some were large enough for two test specimens to be prepared from a single extracted sample. The specimens were tested with their layers intact as the authors found a clear separation of layers of the aneurysms to be impossible. At this point, the thickness of the specimens were measured. A scatter pattern of black dots was then applied to the surface of the specimens using a spray to allow the displacements to be optically measured. To mount the specimens in the biaxial testing mechaine, hooked surgical sutures were used. The specimens were then submerged in a 0.9% physiological saline bath which was heated up to 37 $\pm$ 0.1°C. The tests were conducted using a stretch-driven protocol, starting at 2.5% deformation and increasing in 0.025 stretch steps until rupture. This was carried out at a quasi-static strain rate of 3 mm·min^{-1}, and with a stretch ratio of $\lambda_{axial} : \lambda_{circ} = 1 : 1$, where λ_{axial} is the stretch in the axial direction and λ_{circ} is the stretch in the circumferential direction. Four preconditioning cycles were conducted after each increase in step, with the fifth recorded for data analysis. The results presented in the study by Niestrawska et al. [52] included the Cauchy stress-stretch data in both the axial and circumferential directions of 12 patch specimens. The results displayed large variability in mechanical response. However, despite the variability, when comparing the Cauchy stress at 1.15 stretch, the stresses

in the circumferential direction were consistently higher than the axial direction. The experimental data chosen here was from the specimen with the behaviour that was approximately median out of all the specimens (specimen AAA-1.2).

1.2.2 Constitutive modelling

The studies on modeling the mechanical behavior of biological soft tissues go back to the 19th century. In 1847, M.G. Wortheim presented force-elongation data of femoral arteries and saphenous vein, he noticed that force and elongation are not linearly dependent as Young suggested. Wertheim proposed a constitutive relation of the form

$$\varepsilon = a\sigma^2 + b\sigma \tag{1.1}$$

where a and b are material parameters and ε and σ are strain and stress, respectively [43]. In 1909, Osborne [54] was studied on the urinary bladder and had noticed that the bladder presents a non-linear stiffening under large strain. He recorded that the bladder has a web of elastic fibers, it might be the first work that highlighted the anisotropic fibrous nature of soft tissues. In 1926, Wohlisch had found that collagens shrink with induced heat similar to that in rubberlike materials [30, 43]. Karrer [46] also noticed similarities between soft tissues and rubber-like materials, he tried to find a kinetic theory for a muscle contraction based on a thermo-mechanical analysis of long-chained molecules.

In the early 20th century, advances in rubberlike materials and tissue mechanics have been recorded concurrently. The main reason for the similarity between rubber and soft tissue is that they are each composed of macromolecules. The interested reader is referred to [33] for a detailed explanation of similarities between rubberlike materials and biological soft tissues. Many isotropic models of soft tissues come from rubber-like material studies. However, constitutive models for rubber-like materials are created to model strain-hardening of the material and captured S-shape stress-strain behavior. Fung [25] noted that the stress-strain relation of soft tissue is exponential. Following the evidence of Fung, many isotropic constitutive models were developed in exponential form, also called Fung-form or Fung-type [4, 6, 19, 21, 31, 57, 64, 66, 70]. More accurate constitutive models were proposed by describing anisotropic nature of

tissues. There are three main approaches to describe the anisotropic mechanical behavior of soft tissue. The first one is based on Green-Lagrange strain components, the second one is based on strain invariants, and the third one is based on fiber dispersion. Tong and Fung [67] proposed the first model using the Green-Lagrange strain components. Three years later, Fung [27] introduced a more generic form, and Chuong and Fung [13] extended this generic form to the three-dimensional setting. However, the model of Chuong and Fung was not including shear strain components. Humphrey [42] included shear strain components and global formulation of generic Fung-type strain energy function formed. Choi et al. [12], Kasyanov et al. [47], Costa et al. [16] and Rajagopal et al. [58] proposed Fung-type exponential functions based on Green-Lagrange strain components to model soft tissues. There are also presented constitutive models based on Green-Lagrange strain components but do not have Fung-type exponential form [58, 65, 67, 69]. The main obstacle of constitutive models based on Green-Lagrange strain components is that they have a large number of material parameters. For example, the model of Chuong and Fung [13] has 6, the model of Humphrey [42] has 9 material parameters. Furthermore, these material parameters have no physical meaning and are difficult to identify. Additionally, as Holzapfel et al. [34] indicated in their review, for some parameter sets of Fung model [27], the strain energy is not polyconvex and have a stability issue. Another weak point of constitutive models of tissue based on strain components is that they do not consider tissue histology, this approach is fully phenomenological.

The strain invariant approach on the other hand considers tissue histology. The direction of fibers is included in the analysis via anisotropic strain invariants. In this approach, it is assumed that fibers are perfectly aligned into the ground substance. Humphrey [45] formulated constitutive relation of cardiac tissue based on strain invariants, he additively decomposed free energy function into isotropic and anisotropic parts. The isotropic ground behavior was represented with the model proposed by Demiray [20]. The proposed anisotropic model was based on the square root of the fourth invariant which basically represents the stretch of fiber. Three years later, Humphrey [44] proposed a series form of constitutive relation for passive myocardium based on the first invariant and the square root of the fourth invariant similar to Rivlin's series which is used for isotropic hyperelasticity. Weiss et al. [71] had introduced three dimensional incompressible, transversely isotropic,

hyperelastic constitutive model to describe general biological soft tissues. Mooney-Rivlin model was employed to represent ground material, and the exponential form of the fourth invariant was used to describe the anisotropic part. Newman et al. [51] proposed a constitutive model for the mitral valve, anterior valve, and posterior tissue. The proposed free energy function was analogous to the model of Fung [27]. Instead of using an exponential function of the Green-Lagrange strain component, the exponential of a quadratic function of strain invariants was used. Holzapfel et al. [34] introduced a constitutive model passive mechanical response of arterial wall. The artery was modeled elastic circular tube composed of two layers, and each layer had been treated as a composite material with two families of fibers symmetrically disposed of with the circumferential direction of the artery. Isotropic response of each layer had been determined by neo-Hookean model of Treloar [68]. In order to capture the J-form of stress-strain behavior, an exponential function was used to describe collagen fibers. The model was able to describe the behavior of adventitia and media of arterial wall. Holzapfel et al. [39] extended previously proposed constitutive model [34] to represent each layer of coronary arteries with nonatherosclerotic intimal thickening. A scalar parameter to represent the measure of anisotropy had been introduced. The measure of dispersion parameter is able to calibrate the model between the case of isotropy and transversely isotropy. The model successfully captured the uniaxial strip test data of each layer of a human coronary artery. Alastrue et al. [2] proposed a polynomial potential to model the passive mechanical behavior of the ovine infrarenal vena cava tissue, they also compared the proposed model with the model of Holzapfel et al. [34] and the model of Lin and Yin [49]. Although the model of Lin and Yin [49] showed a better fit, it was not convex. Even the model of Holzapfel et al. [34] was originally proposed to represent the behavior of arterial wall, it accurately described the behavior of vena cava tissue. Ogden and Saccomandi [53] developed a constitutive model for arterial tissue in which the extensibility limit of both collagen fibers and isotropic ground substance is regarded. To describe the isotropic ground material's behavior, Gent model [29] was used. Gent model is one of the simplest phenomenological models of hyperelastic behavior of rubber-like material in which polymer chain extensibility is limited by a material parameter. For the anisotropic part, Ogden and Saccomandi adopted the transversely isotropic model of Horgan and Saccomandi [41] for two families of fibers. The majority of constitu-

tive laws of biological soft tissue are based on strain invariants. Aforementioned the strain invariant approach assumes that fibers are perfectly aligned, however, collagen fibers exist in a dispersed form in the tissue. Fiber dispersion-based models consider tissue histology in a more realistic situation. There are two approaches for describing fiber dispersion [38], (i) angular integration approach and (ii) generalized structure tensor approach. The first fiber dispersion model was presented by Lanir [48]. He proposed a continuum framework to model flat biological tissues, using the angular integration approach and described the distribution of collagen and elastin fibers with Gaussian distribution function. Starting from the study of Lanir, the researchers had extensive effort over modelling the fiber dispersed material with the angular integration approach. Sacks et al. [59] utilized the angular integration approach with beta distribution function to characterize anisotropic behavior of planar collagenous tissue. Zulliger et al. [73] investigated rat carodids and described the dispersion of collagen fibers with log-logistic distribution function. Following the study of Lanir, Billiar et al. [7] and Driessen et al. [22] studied soft tissues containes distributed collagen fibers with Gaussion distribution function. Alasture et al. [1] investigated human arterial wall with von Mises distribution function; they were also conducted the same invesitagation using the Bingham distribution [3]. The generalized structure tensor formulation was introduced by Gasser et al. [28]. The model of Gasser et al. [28] was originally proposed to model arterial walls assuming the out-of-plane distribution of the fibers. Holzapfel et al. [35] extended the model of Gasser et al. [28], and took into account the in-plane dispersion in a more generic form.

As the number of models increased, a need to compare the models became vital. Cortes et al. [15] had compared the AI approach and GST approach for connective tissue. For comparison, free energy function of Holzapfel et al. [34] and von Mises distribution function used by Gasser et al. [28] was selected. It was observed that both formulations have similar performance in terms of describing material behavior. Similar comparisons were also made by Holzapfel and Ogden [37] for human arterial tissue. The result was the same, they concluded that GST and AI approaches are equivalent in terms of fitting performance to experimental tension data. However, they stated that the AI approach is expensive in CPU time since numerical integration is required for every stretch level. On contrary, once the preferred fiber direction and distribution of fibers are known, the generalized structure tensor is obtained and no

further integration is needed.
A summary of the main continuum models discussed above is listed in Table 1.1.

Table 1.1: Overview of main continuum models listed in chronological order of apperance. The colomn 'formulation' describes the approach presented in the cited article (GST, generalized structure tensor; AI, angular integration); the column 'tissue type' name the tissue to which the cited model has been originally applied.

year	**model name**	**formulation**	**tissue type**
1998	NY model [51]	invariant	mitral valve
2000	HGO model [34]	invariant	arterial wall
2005	HSGR [39]	invariant	arterial wall
2005	DBB model [22]	AI	arterial wall-aortic valve
2006	GOH model [28]	GST	arterial wall
2007	OS model [53]	invariant	arterial wall
2009	AMDM model [1]	AI	blood vessel
2010	ASDM model [3]	AI	blood vessel
2015	HNORS model [35]	GST	arterial wall

1.3 Scope and outline

In literature, two types of deformation modes are more common for mechanical characterization of biological soft tissue specimens, namely uniaxial tension (UT) and equibiaxial tension (ET). The UT experiments are carried out in two orthotropic directions in a straightforward manner via universal testing machines [14, 35, 39, 72]. The ET experiments are conducted with the biaxial testing machines with displacement controlled testing protocol [50, 51, 52]. In literature, usually, animal tissues are the subject of experimental studies due to easy access, however, animal tissues and human tissues, in general, have different hyperelastic responses due to differences in collagen orientation [23]. Therefore, using a dataset for human tissue is a good choice to assist human clinical studies. On the other hand, mechanical experiments on human tissues are quite rare, and in some datasets, stretch-stress response

in at least two directions is not available, which is a must for identifying anisotropic response. Therefore, considering the above criteria, we have selected the datasets of Niestrawska et al. [52], Cooney et al. [14], and Martins et al. [50]. These three datasets contain stretch-stress responses for different parts of the human body; the dataset of Niestrawska et al. [52] is for an abdominal aortic aneurysm (AAA) tissue, the dataset of Cooney et al. [14] is for linea alba, and the dataset of Martins et al. [50] is for rectus sheath. AAA is a pathological condition of the abdominal aorta which results in local bulging. Linea alba and rectus sheath are parts of the abdominal wall. The motivation of studies on AAA and the abdominal wall is that these tissues are often subjected to surgical treatment. An accurate representation of the mechanical response of these tissues leads to run successful simulations of surgical procedures and designing proper medical devices.
In this study,

(i) we have outlined 9 hyperelastic models briefly and derive the close-form stress expessions for uniaxial and equibiaxial tension deformation states based on the incompressibility assumption,

(ii) we have implemented 9 hyperelastic constitutive models into hybrid genetic-gradient search algorithm in MATLAB in the sense of Dal et al. [17],

(iii) we have identified the material parameters of each model (i) with respect to ET dataset for AAA tissue [52], (ii) UT dataset for linea alba [14], (iii) UT dataset for rectus sheath [50],

(iv) we have sorted all models with respect to an objective *quality of fit* metric according to their fitting performance to AAA tissue dataset [52], linea alba dataset [14], and rectus sheath dataset [50], respectively.

(v) The identified parameters and the quality of fit values of each constitutive model have been presented in tabular form. The stress-strain curves for each constitutive model have been provided in seperate graphs.

The thesis is organized as follows: Mathematical preliminaries for kinematics of incompressible anisotropic hyperelastic solid are presented in Chapter 2. In Chapter 3,

9 anisotropic hyperelastic constitutive models for biological soft tissue are summarized. Chapter 1.2.1 outlines the experimental observations for biological soft tissues. In Chapter 4, the parameter optimization procedure is presented. The result of the study and conluding remarks is given in Chapter 5.

CHAPTER 2

THEORY

2.1 Fundamental maps and governing equations of motion

In this section, the field equations and corresponding state variables will be the subject of investigation for a hyperelastic tissue in general anisotropic form, with two families of fiber orientations. The theoretical premise and kinematics of the deformations and constitutive equations will be laid.

2.1.1 Geometric mappings and the field variables

2.1.1.1 Kinematics

The deformation of a solid body is driven by the deformation map $\boldsymbol{\varphi}(\boldsymbol{X}, t)$ represents deformation field which maps the reference/Lagrangian configuration $\boldsymbol{X} \in \mathscr{B}_0$ of material point onto the current/Eulerian configuration of material points $\boldsymbol{x} = \boldsymbol{\varphi}_t(\boldsymbol{X})$ at time $t \in \mathscr{T} \subset \mathbb{R}_+$. The *deformation gradient*

$$\boldsymbol{F} : T_X\mathscr{B}_0 \to T_x\mathscr{B}; \quad \boldsymbol{F} := \frac{\partial \boldsymbol{\varphi}_t(\boldsymbol{X})}{\partial \boldsymbol{X}} \tag{2.1}$$

maps the unit tangent of reference configuration onto the spatial counterpart in the current configuration where $T_X\mathscr{B}_0$ and $T_x\mathscr{B}$ denote the tangent spaces in the reference and current configuration. Additionally, let the co-tangent spaces in the the reference and current manifolds are represented as $T_X^*\mathscr{B}_0$ and $T_x^*\mathscr{B}$, respectively. If the cofactor of the deformation gradient is weighted by the volume map/Jacobian $\det[\boldsymbol{F}]$, a normal map per unit reference volume can be obtained between the unit

normals in the undeformed and deformed configurations

$$\boldsymbol{F}^{-T} : T^*_X\mathscr{B}_0 \to T^*_x\mathscr{B}; \quad \boldsymbol{n} = \boldsymbol{F}^{-T}\boldsymbol{N} \tag{2.2}$$

where $\boldsymbol{n}$ is the unit normal vector in reference configuration and $\boldsymbol{N}$ is the unit normal vector in current configuration. In sequel, let line, area, and volume elements in the Lagrangian configurations to be denoted as $d\boldsymbol{X}$, $d\boldsymbol{A}$, dV, respectively. The Eulerian counterparts of these elements are mapped through the deformation gradient $\boldsymbol{F}$, its cofactor $\mathrm{cof}[\boldsymbol{F}] = \det[\boldsymbol{F}]\boldsymbol{F}^{-T}$ and its Jacobian $J := \det[\boldsymbol{F}] > 0$

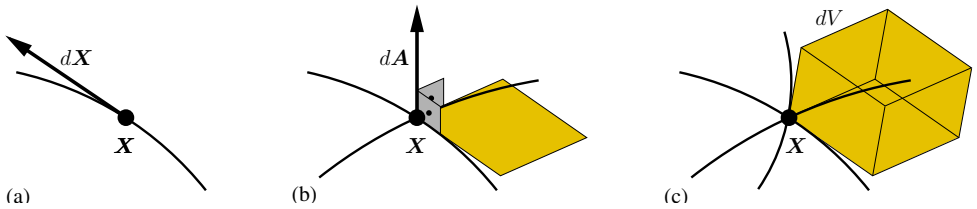

Figure 2.1: Three fundamental maps of a continuum: (a) The deformation gradient $\boldsymbol{F}$ as a mapping of an infinitesimal line element, (b) its cofactor $\mathrm{cof}[\boldsymbol{F}]$ as an area map, and (c) and its determinant $\det[\boldsymbol{F}]$ as a volume map; adopted from [17].

$$d\boldsymbol{x} = \boldsymbol{F}d\boldsymbol{X}\ , \qquad d\boldsymbol{a} = \mathrm{cof}[\boldsymbol{F}]d\boldsymbol{A}\ , \qquad dv = \det[\boldsymbol{F}]dV\ , \tag{2.3}$$

see also Figure 2.1. Having $J := \det[\boldsymbol{F}] > 0$ guarantees the interpenetration of matter to be excluded from the deformation map $\boldsymbol{\varphi}$. To define the mappings between the co and contravariant objects in the Lagrangian an Eulerian manifolds, the manifolds in the undeformed $\mathscr{B}_0$ and deformed $\mathscr{B}$ configurations are locally equipped with covariant $\boldsymbol{G}$ and current $\boldsymbol{g}$ metric tensors in the neighborhoods $\mathcal{N}_X$ of $\boldsymbol{X}$ and $\mathcal{N}_x$ of $\boldsymbol{x}$, respectively. In the sequel, the *right Cauchy Green tensor* and the inverse of the *left Cauchy Green tensors* are defined

$$\boldsymbol{C} = \boldsymbol{F}^T\boldsymbol{g}\boldsymbol{F} \qquad \text{and} \qquad \boldsymbol{c} = \boldsymbol{F}^{-T}\boldsymbol{G}\boldsymbol{F}^{-1} \tag{2.4}$$

as the pull back of the current metric $\boldsymbol{g}$ and push-forward of the Lagrangian metric $\boldsymbol{G}$, respectively.The inverse of the *left Cauchy Green Tensor* is commonly known as the *Finger tensor* and represented as $\boldsymbol{b} = \boldsymbol{c}^{-1}$.

2.1.2 Principal stretches and invariants

For principals of material objectivity and frame indifference to be satisfied, the energy stored in the hyperelastic material should be a function of either principal stretches or invariants of the right Cauchy Green tensor. By writing the spectral decomposition of right Cauchy-Green tensor $\boldsymbol{C}$ and $\mathrm{cof}[\boldsymbol{C}]$ we would obtain the following

$$\boldsymbol{C} := \sum_{a=1}^{3} \lambda_a^2 \boldsymbol{N}^a \otimes \boldsymbol{N}^a \quad \text{and} \quad \mathrm{cof}[\boldsymbol{C}] := \sum_{a=1}^{3} \nu_a^2 \boldsymbol{N}^a \otimes \boldsymbol{N}^a \,, \tag{2.5}$$

where

$$\nu_i = J/\lambda_i \quad \text{with} \quad \nu_1 = \lambda_2\lambda_3 \,, \quad \nu_2 = \lambda_3\lambda_1 \,, \quad \nu_3 = \lambda_1\lambda_2 \,, \tag{2.6}$$

are the *principal areal stretches* and $\boldsymbol{N}^a$ represent the principal directions, see Figure 2.2. Moreover, the three isotropic invariants of the right Cauchy Green tensor are

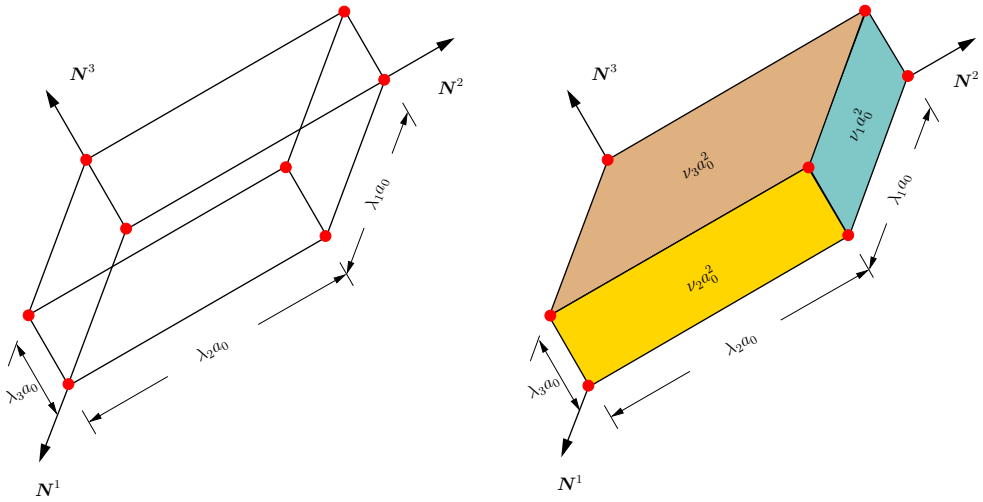

Figure 2.2: The invariants (a) $I_1(\boldsymbol{C}) = \lambda_1^2+\lambda_2^2+\lambda_3^2$ as sum of squares of the principal stretches, (b) $I_2(\boldsymbol{C}) = \nu_1^2+\nu_2^2+\nu_3^2$ as sum of squares of principal areal stretches where $\nu_i = J/\lambda_i$ and (c) $I_3 = J^2 = \lambda_1^2\lambda_2^2\lambda_3^2$ as square of volumetric stretch; adopted from [17].

$$I_1 := \mathrm{tr}[\boldsymbol{C}], \quad I_2 := \mathrm{tr}[\mathrm{cof}[\boldsymbol{C}]], \quad \text{and} \quad I_3 := \det[\boldsymbol{C}] \,. \tag{2.7}$$

The principal stretches and the invariants of the right Cauchy Green stretch tensor are related as through

$$I_1 = \lambda_1^2 + \lambda_2^2 + \lambda_3^2, \quad I_2 = \nu_1^2 + \nu_2^2 + \nu_3^2, \quad I_3 = J^2 = \lambda_1^2\lambda_2^2\lambda_3^2 \,. \tag{2.8}$$

If a material point is depicted by an infinitesimal cubic element, the squares of its *linear*, *areal*, and *volumetric* stretches are associated with the three isotropic invariants of the right Cauchy Green stretch tensor. In describing the anisotropic behavior of soft tissues, four additional invariants are typically defined to take into account the contribution of the preferential initial fiber alignment

$$\begin{aligned} I_4 &:= \boldsymbol{M}_1.\boldsymbol{C}\boldsymbol{M}_1 \qquad \text{and} \qquad I_5 := \boldsymbol{M}_1.\boldsymbol{C}^2\boldsymbol{M}_1 \,, \\ I_6 &:= \boldsymbol{M}_2.\boldsymbol{C}\boldsymbol{M}_2 \qquad \text{and} \qquad I_7 := \boldsymbol{M}_2.\boldsymbol{C}^2\boldsymbol{M}_2 \,, \end{aligned} \tag{2.9}$$

where $\boldsymbol{M}_1$ and $\boldsymbol{M}_2$ are the unit fiber orientation vectors of the first family of fibers and the second family of ribers in reference configuration, respectively. $\sqrt{I_4}$ and $\sqrt{I_6}$ represents the stretch of fibers in the direction $\boldsymbol{M}_1$ and $\boldsymbol{M}_2$, respectively, however I_5 and I_7 have no similar physical representation. In sequel, orientation vectors of two families of fibers, symmetrically disposed in the $\boldsymbol{e}_1 - \boldsymbol{e}_2$ plane in current configuration are

$$\boldsymbol{m}_1 = \boldsymbol{F}\boldsymbol{M}_1 \qquad \text{and} \qquad \boldsymbol{m}_2 = \boldsymbol{F}\boldsymbol{M}_2 \,. \tag{2.10}$$

Morover, the second order structural tensor can be defined as

$$\boldsymbol{A}_1 = \boldsymbol{M}_1 \otimes \boldsymbol{M}_1 \qquad \text{and} \qquad \boldsymbol{A}_2 = \boldsymbol{M}_2 \otimes \boldsymbol{M}_2 \,. \tag{2.11}$$

The second order structural tensor can be expressed in current configuration as follows

$$\boldsymbol{a}_1 = \boldsymbol{m}_1 \otimes \boldsymbol{m}_1 \qquad \text{and} \qquad \boldsymbol{a}_2 = \boldsymbol{m}_2 \otimes \boldsymbol{m}_2 \,. \tag{2.12}$$

2.1.3 Free energy function

Hyperelasticity is the term to define material which produces no entropy. In other words, hyperelastic material dissipates not energy, therefore, their material response is governed by a single energy function which describes the stored energy by the material; this energy function is known as Helmholtz free energy function, or strain energy density function. Since some materials behave differently in bulk deformation and shear deformation, it is common practice to split the deformation into a volume-changing and an volume-preserving part according to

$$\boldsymbol{F} = \boldsymbol{F}_{vol}\bar{\boldsymbol{F}} \quad \text{with} \quad \boldsymbol{F}_{vol} := J^{1/3}\boldsymbol{1} \,. \tag{2.13}$$

The corresponding strain measure reads

$$\boldsymbol{C} = (J^{2/3}\mathbf{1})\bar{\boldsymbol{C}} \quad \text{with} \quad \bar{\boldsymbol{C}} = \bar{\boldsymbol{F}}^T\bar{\boldsymbol{F}}\,. \tag{2.14}$$

Based on 2.13 and 2.14, the free energy function is expressed as

$$\psi = U(J) + \bar{\psi}(\bar{\boldsymbol{F}}, \boldsymbol{A}_1, \boldsymbol{A}_2) \tag{2.15}$$

where $U(J)$ and $\bar{\psi}(\bar{\boldsymbol{F}}, \boldsymbol{A}_1, \boldsymbol{A}_2)$ represent volumetric and isochoric response of material, respectively. Further decomposition of isochoric free energy function was suggested by Holzapfel and Weizsacker [40]. They proposed decomposition of free energy function into isotropic and anisotropic parts,

$$\bar{\psi}(\bar{\boldsymbol{F}}, \boldsymbol{A}_1, \boldsymbol{A}_2) = \bar{\psi}_{iso}(\bar{\boldsymbol{F}}) + \bar{\psi}_{ani}(\bar{\boldsymbol{F}}, \boldsymbol{A}_1, \boldsymbol{A}_2)\,. \tag{2.16}$$

The wavy collagen fibers do not store energy at low pressures, hence, isotropic ground matrix is active with $\bar{\psi}_{iso}$ at low stresses. In contrary, the collagen fibers dominate the overall behavior at large stresses and this is governed by $\bar{\psi}_{ani}$.

2.2 Stress expressions

Assuming zero dissipation in hyperelastic solids leads to the canonical relation between the Lagrangian/Eulerian stresses and the free energy function in the sense

$$\boldsymbol{S} = 2\partial_{\boldsymbol{C}}\hat{\psi}(\boldsymbol{C}, \boldsymbol{A}_1, \boldsymbol{A}_2) \quad \text{and} \quad \boldsymbol{\tau} = 2\partial_{\boldsymbol{g}}\tilde{\psi}(\boldsymbol{g}, \boldsymbol{F}, \boldsymbol{A}_1, \boldsymbol{A}_2)\,. \tag{2.17}$$

Herein, $\boldsymbol{S}$ and $\boldsymbol{\tau}$ are the second Piola-Kirchhoff and the Kirchhoff stresses, respectively.

2.2.1 Invariant formulations

For the case of anisotropic elasticity, for the case of invariant-based free energy function, by applying the chain rule we will obtain the Lagrangian and Eulerian stress descriptions as

$$\boldsymbol{S} = 2\partial_{\boldsymbol{C}}\psi = 2\sum_{i=1}^{7}\frac{\partial\psi}{\partial I_i}\frac{\partial I_i}{\partial \boldsymbol{C}}, \tag{2.18}$$

$$\boldsymbol{\tau} = 2\partial_{\boldsymbol{g}}\psi = 2\sum_{i=1}^{7} \frac{\partial \psi}{\partial I_i}\frac{\partial I_i}{\partial \boldsymbol{g}} \,. \tag{2.19}$$

The closed form expressions for the Lagrangian and Eulerian stress tensors in (2.18) and (2.19) require the following derivatives

$$\begin{aligned} &\partial_{\boldsymbol{C}} I_1 = \boldsymbol{1} \,, \quad \partial_{\boldsymbol{C}} I_2 = I_1 \boldsymbol{1} - \boldsymbol{C} \,, \quad \partial_{\boldsymbol{C}} J = \tfrac{1}{2}\, J \boldsymbol{C}^{-1} \,, \\ &\partial_{\boldsymbol{C}} I_4 = \boldsymbol{A}_1 \,, \quad \partial_{\boldsymbol{C}} I_5 = \boldsymbol{M}_1 \otimes \boldsymbol{C}\boldsymbol{M}_1 + \boldsymbol{M}_1 \boldsymbol{C} \otimes \boldsymbol{M}_1 \,, \\ &\partial_{\boldsymbol{C}} I_6 = \boldsymbol{A}_2 \,, \quad \partial_{\boldsymbol{C}} I_7 = \boldsymbol{M}_2 \otimes \boldsymbol{C}\boldsymbol{M}_2 + \boldsymbol{M}_2 \boldsymbol{C} \otimes \boldsymbol{M}_2 \,. \end{aligned} \tag{2.20}$$

The derivatives with respect to the spatial metric $\boldsymbol{g}$ follows from the push-forward operation of (2.20), i.e.

$$\begin{aligned} &\partial_{\boldsymbol{g}} I_1 = \boldsymbol{b} \,, \quad \partial_{\boldsymbol{g}} I_2 = I_1 \boldsymbol{b} - \boldsymbol{b}^2 \,, \quad \partial_{\boldsymbol{g}} J = \tfrac{1}{2}\, J \boldsymbol{g}^{-1} \,, \\ &\partial_{\boldsymbol{g}} I_4 = \boldsymbol{a}_1 \,, \quad \partial_{\boldsymbol{g}} I_5 = \boldsymbol{m}_1 \otimes \boldsymbol{b}\boldsymbol{m}_1 + \boldsymbol{m}_1 \boldsymbol{b} \otimes \boldsymbol{m}_1 \,, \\ &\partial_{\boldsymbol{g}} I_6 = \boldsymbol{a}_2 \,, \quad \partial_{\boldsymbol{g}} I_7 = \boldsymbol{m}_2 \otimes \boldsymbol{b}\boldsymbol{m}_2 + \boldsymbol{m}_2 \boldsymbol{b} \otimes \boldsymbol{m}_2 \,. \end{aligned} \tag{2.21}$$

Substitution of (2.20) and (2.21) into (2.18) and (2.19), then rearranging the terms finally gives the invariant based representation of stresses for anisotropic hyperelastic solid

$$\begin{aligned} \boldsymbol{S} \;&=\; 2(c_1 + I_1 c_2)\boldsymbol{1} - 2c_2 \boldsymbol{C} + 2c_3 \boldsymbol{A}_1 + 2c_4(\boldsymbol{M}_1 \otimes \boldsymbol{C}\boldsymbol{M}_1 + \boldsymbol{M}_1 \boldsymbol{C} \otimes \boldsymbol{M}_1) \\ &+\; 2c_5 \boldsymbol{A}_2 + 2c_6(\boldsymbol{M}_2 \otimes \boldsymbol{C}\boldsymbol{M}_2 + \boldsymbol{M}_2 \boldsymbol{C} \otimes \boldsymbol{M}_2) - p\boldsymbol{C}^{-1} \,, \end{aligned} \tag{2.22}$$

$$\begin{aligned} \boldsymbol{\tau} \;&=\; 2(c_1 + I_1 c_2)\, \boldsymbol{b} - 2c_2 \boldsymbol{b}^2 + 2c_3 \boldsymbol{a}_1 + 2c_4(\boldsymbol{m}_1 \otimes \boldsymbol{b}\boldsymbol{m}_1 + \boldsymbol{m}_1 \boldsymbol{b} \otimes \boldsymbol{m}_1) \\ &+\; 2c_5 \boldsymbol{a}_2 + 2c_6(\boldsymbol{m}_2 \otimes \boldsymbol{b}\boldsymbol{m}_2 + \boldsymbol{m}_2 \boldsymbol{b} \otimes \boldsymbol{m}_2) - p\boldsymbol{g}^{-1} \,. \end{aligned} \tag{2.23}$$

with

$$\begin{aligned} &c_1 = \frac{\partial \psi}{\partial I_1} \,, \quad c_2 = \frac{\partial \psi}{\partial I_2} \,, \quad c_3 = \frac{\partial \psi}{\partial I_4} \,, \\ &c_4 = \frac{\partial \psi}{\partial I_5} \,, \quad c_5 = \frac{\partial \psi}{\partial I_6} \,, \quad c_6 = \frac{\partial \psi}{\partial I_7} \,, \quad p = -J\partial_J \psi \,. \end{aligned} \tag{2.24}$$

The stress expressions given in (2.22) and (2.23) can be expressed in terms of index notation for principal directions ,

$$\begin{aligned} S_i &= 2(c_1 + I_1 c_2) - 2c_2\lambda_i^2 + 2c_3 M_{1_i}^2 + 4c_4 M_{1_i}^2 \lambda_i^2 \\ &+ 2c_5 M_{2_i}^2 + 4c_6 M_{2_i}^2 \lambda_i^2 - \frac{1}{\lambda_i^2} p\,, \\ \tau_i &= 2(c_1 + I_1 c_2)\lambda_i^2 - 2c_2\lambda_i^4 + 2c_3 m_{1_i}^2 \lambda_i^2 + 4c_4 m_{1_i}^2 \lambda_i^4 \\ &+ 2c_5 m_{2_i}^2 \lambda_i^2 + 4c_6 m_{2_i}^2 \lambda_i^4 - p\,. \end{aligned} \tag{2.25}$$

2.2.2 Fiber dispersion formulation

Fiber dispersion based modelling approaches utilize probability density function concept to represent fiber architecture of tissues. If arbitrary unit fiber direction is $\boldsymbol{r}$ in undeformed configuration, the probability of finding fibers in $\boldsymbol{r}$ direction is expressed with $\rho(\boldsymbol{r})$, then the free energy of fibers in $\boldsymbol{r}$ direction is given by ψ_f. The arbitrary fiber orientation vector can be expressed in spherical coordinates as follows

$$\boldsymbol{r} = \sin\Theta\cos\Phi \boldsymbol{e}_1 + \sin\Theta\sin\Phi \boldsymbol{e}_2 + \cos\Theta \boldsymbol{e}_3\,. \tag{2.26}$$

The Eulerian counterpart of $\boldsymbol{r}$ is computed with push forward operation $\boldsymbol{t} = \boldsymbol{F}\boldsymbol{r}$, and expressed in spherical coordinates as follows

$$\boldsymbol{t} = \lambda_1 \sin\Theta\cos\Phi \boldsymbol{e}_1 + \lambda_2 \sin\Theta\sin\Phi \boldsymbol{e}_2 + \lambda_3 \cos\Theta \boldsymbol{e}_3\,. \tag{2.27}$$

As aforementioned, two different approaches can be used to model the hyperelastic behavior of soft tissues,(i) the generalized structure tensor approach, and (ii) the angular integration approach.

2.2.2.1 Generalized structure tensor formulation

Generalized structure tensor is defined as

$$\mathbf{H} = \frac{1}{4\pi} \int_\Omega \rho(\boldsymbol{r}) \boldsymbol{r} \otimes \boldsymbol{r} \mathrm{d}\Omega \tag{2.28}$$

with $\mathrm{tr}\mathbf{H} = 1$, resulted from normalization condition. The generalized structure tensor is an average of individual structure tensor $\boldsymbol{r}\otimes\boldsymbol{r}$. For the case of generalized structure tensor formulations, by applying the chain rule we will obtain the Lagrangian and

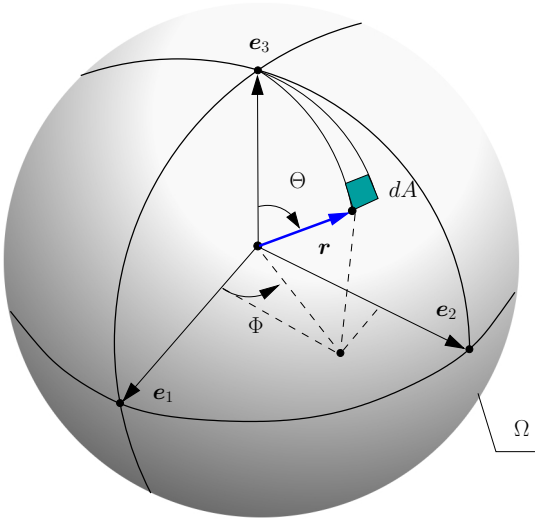

Figure 2.3: The unit micro-sphere and the arbitrary fiber orientation vector $\boldsymbol{r} = r_1\boldsymbol{e}_1 + r_2\boldsymbol{e}_2 + r_3\boldsymbol{e}_3$ where $r_1 = \cos\Phi\sin\Theta$, $r_2 = \sin\Phi\sin\Theta$ and $r_3 = \cos\Theta$ in terms of spherical coordinates $\{\Phi, \Theta\}$, respectively; adopted from [17]

Eulerian stress descriptions as

$$\boldsymbol{S} = 2\partial_{\boldsymbol{C}}\psi = 2\left[\frac{\partial\psi_{iso}}{\partial I_1}\frac{\partial I_1}{\partial \boldsymbol{C}} + \frac{\partial\psi_{iso}}{\partial J}\frac{\partial J}{\partial \boldsymbol{C}} + \frac{\partial\psi_{ani}}{\partial \boldsymbol{E}}\frac{\partial \boldsymbol{E}}{\partial \boldsymbol{C}}\right], \tag{2.29}$$

$$\boldsymbol{\tau} = 2\partial_{\boldsymbol{g}}\psi = 2\left[\frac{\partial\psi_{iso}}{\partial I_1}\frac{\partial I_1}{\partial \boldsymbol{g}} + \frac{\partial\psi_{iso}}{\partial J}\frac{\partial J}{\partial \boldsymbol{g}} + \frac{\partial\psi_{ani}}{\partial \boldsymbol{E}}\frac{\partial \boldsymbol{E}}{\partial \boldsymbol{g}}\right], \tag{2.30}$$

where $\boldsymbol{E} = \boldsymbol{H} : \boldsymbol{C} - 1$. The closed form expressions for the Lagrangian and Eulerian stress tensor require following derivative

$$\partial_{\boldsymbol{C}}\boldsymbol{E} = \boldsymbol{H}. \tag{2.31}$$

The push forward operation of (2.31) follows

$$\partial_{\boldsymbol{g}}\boldsymbol{E} = \boldsymbol{h}. \tag{2.32}$$

Substituting of (2.20), (2.21), (2.31), and (2.32) into (2.29) and (2.30) and rearranging the terms finally gives the generalized structure tensor based representation of stresses for anisotropic hyperelastic solid

$$\boldsymbol{S} = 2c_1\boldsymbol{1} + 2\psi_f'\boldsymbol{H} - p\boldsymbol{C}^{-1}, \tag{2.33}$$

$$\boldsymbol{\tau} = 2c_1\boldsymbol{b} + 2\psi_f'\boldsymbol{h} - p\boldsymbol{g}^{-1}. \tag{2.34}$$

with

$$\psi_f' = \frac{\partial \psi_{ani}}{\partial E}\,. \tag{2.35}$$

In principle directions, (2.33) and (2.34) can be written in terms of principal stretches,

$$S_i = 2c_1 + 2\psi_f' H_i - \frac{1}{\lambda_i^2} p\,, \tag{2.36}$$

$$\tau_i = 2c_1\lambda_i^2 + 2\psi_f' h_i - p\,. \tag{2.37}$$

2.2.2.2 Angular integration formulations

The total free energy of fibers is calculated by

$$\Psi_{ani} = \frac{1}{4\pi}\int_\Omega \rho(\boldsymbol{r})\psi_f \mathrm{d}\Omega \tag{2.38}$$

where Ω represents a unit sphere. Starting with the free energy (2.38), Eulerian stress tensor follows by the application of chain rule

$$\boldsymbol{\tau} = 2\left[\frac{\partial \psi_{ani}}{\partial \lambda_f}\frac{\partial \lambda_f}{\partial \boldsymbol{g}} + \frac{\partial \psi_{iso}}{\partial J}\frac{\partial J}{\partial \boldsymbol{g}} + \frac{\partial \psi_{iso}}{\partial I_1}\frac{\partial I_1}{\partial \boldsymbol{g}}\right]\,. \tag{2.39}$$

Insertion of (2.20), (2.21) and $2\partial_{\boldsymbol{g}}\lambda_f = \lambda_f^{-1}\boldsymbol{t}\otimes\boldsymbol{t}$ into (2.39) gives the Kirchhoff stress expression

$$\boldsymbol{\tau} = n\int_\Omega \rho(\boldsymbol{r})\lambda_f^{-1}\psi_f'\boldsymbol{t}\otimes\boldsymbol{t}\mathrm{d}\Omega + 2c_1\boldsymbol{b} - p\boldsymbol{g}^{-1}\,. \tag{2.40}$$

The general form of Kirchhoff stress for based on angular integration formulation is given in (2.40). In principle directions, (2.40) can be written in terms of principal stretches,

$$\begin{aligned}\tau_1 &= n\lambda_1^2\textstyle\int_\Omega \rho(\boldsymbol{r})\lambda_f^{-1}\psi_f'\cos^2\Phi\sin^3\Theta\mathrm{d}\Theta\mathrm{d}\Phi \\ &+ 2c_1\lambda_1^2 - p\,,\end{aligned} \tag{2.41}$$

$$\begin{aligned}\tau_2 &= n\lambda_2^2\textstyle\int_\Omega \rho(\boldsymbol{r})\lambda_f^{-1}\psi_f'\sin^2\Phi\sin^3\Theta\mathrm{d}\Theta\mathrm{d}\Phi \\ &+ 2c_1\lambda_2^2 - p\,,\end{aligned} \tag{2.42}$$

$$\begin{aligned}\tau_3 &= n\lambda_3^2\textstyle\int_\Omega \rho(\boldsymbol{r})\lambda_f^{-1}\psi_f'\cos^2\Theta\sin\Phi\mathrm{d}\Theta\mathrm{d}\Phi \\ &+ 2c_1\lambda_3^2 - p\,.\end{aligned} \tag{2.43}$$

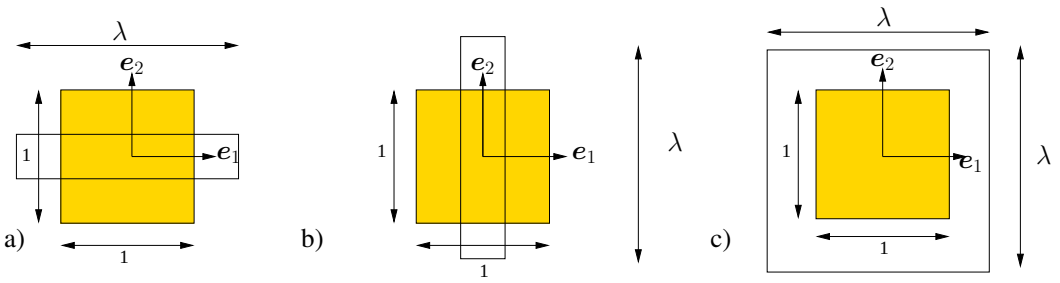

Figure 2.4: Deformation modes - a) uniaxial tension in $\boldsymbol{e}_1$, b) uniaxial tension in in $\boldsymbol{e}_2$, c) equibiaxial tension; updated from [17]

2.2.3 Stresses under homogeneous deformations

The deformation gradient and the nominal stress expression under homogeneous uniaxial, equibiaxial pure shear deformations can be expressed as follows

$$\boldsymbol{F} = \begin{bmatrix} F_{11} & 0 & 0 \\ 0 & F_{22} & 0 \\ 0 & 0 & F_{33} \end{bmatrix} \quad \text{and} \quad \boldsymbol{P} = \begin{bmatrix} P_1 & 0 & 0 \\ 0 & P_2 & 0 \\ 0 & 0 & P_3 \end{bmatrix} . \tag{2.44}$$

Uniaxial tension: For an incompressible anisotropic hyperelastic solid, the deformation and stress states under uniaxial tension are

$$\boldsymbol{F} = \begin{bmatrix} \lambda_1 & 0 & 0 \\ 0 & \lambda_2 & 0 \\ 0 & 0 & \lambda_1^{-1}\lambda_2^{-1} \end{bmatrix} \quad \text{and} \quad \boldsymbol{P} = \begin{bmatrix} P_1 & 0 & 0 \\ 0 & 0 & 0 \\ 0 & 0 & 0 \end{bmatrix} \tag{2.45}$$

see Figure 2.4(a),(b).

Deformation gradient tensor of anisotropic materials cannot be expressed straightforward manner as can be done for isotropic materials, since the amount of contraction in the transverse direction depends on the anisotropic fiber structure. Therefore, the deformation gradient tensor should be obtained iteratively to satisfy equilibrium conditions, $P_{22} = P_{33} = 0$. However, if the mean fiber direction coincides with a principle direction, the deformation gradient tensor used for the isotropic case can be utilized, since the fibers are assumed not to support the compressive load. The deformation gradient tensor for the anisotropic soft tissue which has preferred fiber

direction coincided with principal axes can be written as

$$\boldsymbol{F} = \begin{bmatrix} \lambda & 0 & 0 \\ 0 & \frac{1}{\sqrt{\lambda}} & 0 \\ 0 & 0 & \frac{1}{\sqrt{\lambda}} \end{bmatrix} . \tag{2.46}$$

The first two invariants under uniaxial deformation read

$$I_1 = \lambda_1^2 + \lambda_2^2 + (\lambda_1 + \lambda_2)^{-2} \quad \text{and} \quad I_2 = \lambda_1^2(\lambda_2^2 + \frac{1}{\lambda_2^2}) . \tag{2.47}$$

For symmetrically orthotropic fibers, $I_4 = I_6$ and $I_5 = I_7$ read

$$I_4 = I_6 = \lambda_1^2 \text{cos}^2\varphi + \lambda_2^2 \text{sin}^2\varphi \quad \text{and} \quad I_5 = I_7 = \lambda_1^4 \text{cos}^2\varphi + \lambda_2^4 \text{sin}^2\varphi \tag{2.48}$$

where φ is the angle between the fiber and $\boldsymbol{e}_2$ direction.
The nominal stress $\boldsymbol{P} = \boldsymbol{F}^{-T}\boldsymbol{\tau}$ expression under uniaxial loading for invariant, generalized structure tensor and angular integration based formulations read

$$\begin{aligned}
\text{(UT)} \quad \text{Invariant :} \qquad P_1 &= 2(c_1 + I_1 c_2)\lambda - 2c_2\lambda^3 + 2c_3 m_{1_1}^2 \lambda + 4c_4 m_{1_1}^2 \lambda^3 \\
&+ 2c_5 m_{2_1}^2 \lambda + 4c_6 m_{2_1}^2 \lambda^3 - \frac{1}{\lambda} p , \\
\text{(UT)} \quad \text{GST :} \qquad P_1 &= 2c_1\lambda + 2\psi_f' H_1 \lambda - \frac{1}{\lambda} p , \\
\text{(UT)} \quad \text{AI :} \qquad P_1 &= n\lambda \textstyle\int_\Omega \rho(\boldsymbol{r}) \lambda_f^{-1} \psi_f' \text{cos}^2\Phi \text{sin}^3\Theta \text{d}\Theta\text{d}\Phi \\
&+ 2c_1\lambda - \frac{1}{\lambda} p ,
\end{aligned} \tag{2.49}$$

Equibiaxial tension: For an incompressible hyperelastic solid, the deformation and stress states under equibiaxial tension are

$$\boldsymbol{F} = \begin{bmatrix} \lambda & 0 & 0 \\ 0 & \lambda & 0 \\ 0 & 0 & \lambda^{-2} \end{bmatrix} \quad \text{and} \quad \boldsymbol{P} = \begin{bmatrix} P_1 & 0 & 0 \\ 0 & P_2 & 0 \\ 0 & 0 & 0 \end{bmatrix} . \tag{2.50}$$

see Figure 2.4(c).
The first two invariants under equibiaxial deformation read

$$I_1 = 2\lambda^2 + \frac{1}{\lambda^4} , \quad I_2 = \lambda^4 + \frac{2}{\lambda^2} . \tag{2.51}$$

The invariants related with anisotropy are

$$I_4 = I_6 = \lambda^2 \cos^2\varphi + \lambda^2 \sin^2\varphi \quad \text{and} \quad I_5 = I_7 = \lambda^4 \cos^2\varphi + \lambda^4 \sin^2\varphi \,. \tag{2.52}$$

The nominal stress under equibiaxial loading for invariant, generalized structure tensor and angular integration based formulations read

$$\begin{aligned}
\text{(ET)} \quad \text{Invariant :} \qquad P_1 &= 2(c_1 + I_1 c_2)\lambda - 2c_2\lambda^3 + 2c_3 m_{1_1}^2 \lambda + 4c_4 m_{1_1}^2 \lambda^3 \\
&+ 2c_5 m_{2_1}^2 \lambda + 4c_6 m_{2_1}^2 \lambda^3 - \frac{1}{\lambda} p \,, \\
P_2 &= 2(c_1 + I_1 c_2)\lambda - 2c_2\lambda^3 + 2c_3 m_{2_1}^2 \lambda + 4c_4 m_{2_1}^2 \lambda^3 \\
&+ 2c_5 m_{2_2}^2 \lambda + 4c_6 m_{2_2}^2 \lambda^3 - \frac{1}{\lambda} p \,, \\
\text{(ET)} \quad \text{GST :} \qquad P_1 &= 2c_1\lambda + 2\psi_f' H_1 \lambda - \frac{1}{\lambda} p \,, \\
P_2 &= 2c_1\lambda + 2\psi_f' H_2 \lambda - \frac{1}{\lambda} p \,, \\
\text{(ET)} \quad \text{AI :} \qquad P_1 &= n\lambda \textstyle\int_\Omega \rho(\boldsymbol{r}) \lambda_f^{-1} \psi_f' \cos^2\Phi \sin^3\Theta \mathrm{d}\Theta \mathrm{d}\Phi \\
&+ 2c_1\lambda - \frac{1}{\lambda} p \,, \\
P_2 &= n\lambda \textstyle\int_\Omega \rho(\boldsymbol{r}) \lambda_f^{-1} \psi_f' \sin^2\Phi \sin^3\Theta \mathrm{d}\Theta \mathrm{d}\Phi \\
&+ 2c_1\lambda - \frac{1}{\lambda} p \,.
\end{aligned} \tag{2.53}$$

CHAPTER 3

HYPERELASTIC MATERIAL MODELS

In sequel we will review a common isotropic model and 9 anisotropic hyperelastic model under two main catergories: (i) strain-invariant based models, and (ii) fiber dispersion based models. The free erngy functions and necessary derivatives for stress expressions are outlined.

3.1 Invariant based models

The invariant based models assume perfect alligment of fibers embedded into isotropic ground matrix. Models have been presented for symmetrically disposed two families of fibers.

3.1.1 neo-Hookean model

The neo-Hookean model is the most fundamental model for hyperelastic constitutive models. Many researchers represent the isotropic ground matrix of soft tissues by neo-Hookean model [1, 3, 34, 39, 71]. Therefore, it deserves a seperate description. Based on Wall's treatment of elasticity of a molecular network, Treloar [68] proposed following free energy function

$$\psi = \frac{1}{2} n k_B \theta \left(\lambda_1^2 + \lambda_2^2 + \lambda_3^2 - 3 \right) \tag{3.1}$$

in order to describe the homogeneous deformation of rubber. In 3.1, n is the volume specific chain density, k_B is the Boltzmann constant and θ is the absolute temperature.

Notice that, with shear modulus $\mu = nk_B\theta$, the model can be written as

$$\psi = \frac{\mu}{2}\left(I_1 - 3\right). \tag{3.2}$$

The nonzero derivative of ψ with respect to the invariants is

$$c_1 := \frac{\partial \psi}{\partial I_1} = \frac{\mu}{2}. \tag{3.3}$$

3.1.2 Newman-Yin (NY) model

Newman and Yin [51] proposed a exponential free energy form analogous to proposed by Fung et al. [27] to describe hyperelastic behavior of mitral valve tissue. They assumed that the material is transversely isotropic and the free energy function depends on the first and the fourth invariants. They observed that for constant I_4, both $\frac{\partial \psi}{\partial I_1}$ and $\frac{\partial \psi}{\partial I_4}$ increase nonlinearly. Therefore, Newman and Yin proposed,

$$\psi = k_0(\exp(Q) - 1) \tag{3.4}$$

where Q is the quadratic function of invariants

$$Q = (k_1(I_1 - 3)^2 + k_2(\sqrt{I_4} - 1)^4). \tag{3.5}$$

In order to have a strain energy increases with increasing I_4, k_0 should be positive. Also, if the tissue is not able to support compressive load, k_2 should be positive. The original model was proposed for the material with one family of fiber. However, we have extended the formulation considering two families of fibers,

$$Q = (k_1(I_1 - 3)^2 + k_2(\sqrt{I_4} - 1)^4 + k_2(\sqrt{I_6} - 1)^4). \tag{3.6}$$

The nonzeros derivatives of ψ with respect to invariants are

$$\begin{aligned} c_1 &= 2k_0k_1(I_1 - 3)\exp(Q), \\ c_3 &= 2k_0k_2\exp(Q)\frac{1}{\sqrt{I_4}}(\sqrt{I_4} - 1)^3, \\ c_6 &= 2k_0k_2\exp(Q)\frac{1}{\sqrt{I_6}}(\sqrt{I_6} - 1)^3. \end{aligned} \tag{3.7}$$

3.1.3 Holzapfel-Gasser-Ogden (HGO) model

Holzapfel et al. [34] proposed a constitutive model for model artery. They additively split to isochoric free energy function into isotropic and anisotropic part,

$$\psi = \psi_{iso}(I_1) + \psi_{ani}(I_4, I_6)\,. \tag{3.8}$$

They utilized neo-Hookean model for isotropic part since collagen fibers do not contribute to mechanical behavior of the tissue at low pressures. The free energy stored by two families of collagen fibers described as

$$\psi_{ani}(I_4, I_6) = \frac{k_1}{2k_2} \sum_{i=4,6} \left(\exp[k_2(I_i - 1)^2] - 1\right) \tag{3.9}$$

where $k_1 > 0$ is a stress-like parameter and $k_2 > 0$ is a dimensionless parameter. The collagen fibers do not support compressive stresses due to their wavy nature. Therefore, the anisotropic free energy do not included to total free energy when I_4 and I_6 are less than 1. The nonzeros derivatives of ψ with respect to invariants are

$$\begin{aligned} c_1 &= \frac{c}{2} \\ c_3 &= 2k_1(I_4 - 1)\exp\left(k_2(I_4 - 1)^2 - 1\right) \\ c_5 &= 2k_1(I_6 - 1)\exp\left(k_2(I_6 - 1)^2 - 1\right)\ . \end{aligned} \tag{3.10}$$

3.1.4 Holzapfel-Sommer-Gasser-Regitnig (HSGR) model

Holzapfel et al. [39] proposed a free energy function of the form $\psi(I_1, I_4) = \psi_{iso}(I_1) + \psi_{ani}(I_1, I_4)$. They used classical neo-Hookean model as isotropic part of free energy function. The proposed free energy function is

$$\psi = \mu(I_1 - 3) + \frac{k_1}{k_2}\left(\exp\{k_2[(1-p)(I_1 - 3)^2 + p(I_4 - 1)^2]\} - 1\right)\ , \tag{3.11}$$

where $k_1 > 0$ is stresslike parameter and $k_2 >$ is dimensionless parameter. Even the model 3.11 is classified as an invariant based model, the model accounts for the fiber dispersion phenomenologically by dimensionless parameter $p \in [0, 1]$. p is measure of anisotropy. If $p = 1$, the model reduces to HGO model. If $p = 0$, the fiber related terms drop and the model reduces to an isotropic model. The nonzero derivatives of

the free energy function are

$$
\begin{aligned}
c_1 &= \mu + 2k_1(1-p)(I_1-3)\text{exp}\{k_2[(1-p)(I_1-3)^2 + p(I_4-1)^2]\} \\
c_3 &= 2\frac{k_1}{k_2}p(I_4-1)\text{exp}\{k_2[(1-p)(I_1-3)^2 + p(I_4-1)^2]\}\,.
\end{aligned}
\tag{3.12}
$$

3.1.5 Ogden-Saccomandi (OS) model

Ogden and Saccomandi [53] proposed a logarithmic constitutive law for arterial tissue in which the fiber extension is limited. They additively decomposed the free energy function into isotropic and anisotropic parts,

$$\psi = \psi_{iso}(I_1) + \psi_{ani}(I_4, I_6)\,. \tag{3.13}$$

To model the isotropic behavior of the tissue, they adopted well known rubber elasticity model of Gent [29] which limits the chain extensibility. The free energy function of Gent model is

$$\psi_{iso} = -\frac{1}{2}\mu J_m \text{log}\left(1 - \frac{I_1 - 3}{J_m}\right)\,, \tag{3.14}$$

where μ is shear modulus. J_m is the parameter that account of limiting polymeric chain extensibility which anologously used in the context of soft tissue. J_m limits the extensibility by limiting the value of $I_1 - 3$, and mathematically the logarithm in 3.14 can be defined if the deformation satisfies the constraint,

$$I_1 < 3 + J_m\,. \tag{3.15}$$

If $J_m \to \infty$, 3.14 reduces to neo-Hookean model. Similar model of 3.14 was proposed by Horgan and Saccomandi [41] for transversely isotropic material. Instead of limiting polymer chain extensibility, model of Horgan and Saccomandi limits the extensibility of fibers. Ogden and Saccomandi adopted the model of Horgan and Saccomandi for arterial tissue with two families of fibers. The anisotropic free energy used by Ogden and Saccomandi is

$$\psi_{ani} = -\frac{k_1}{2}J_f \sum_{\alpha=4,6} \text{log}\left(1 - \frac{(I_\alpha - 1)^2}{J_f}\right)\,, \tag{3.16}$$

where k_1 is the stresslike parameter, and J_f is the limiting parameter of extensibility of collagen fibers. The counterpart of contraint 3.15 should be satisfied,

$$I_\alpha < \sqrt{J_f} + 1\,, \quad \alpha = 4, 6\,. \tag{3.17}$$

The nonzero derivatives of free energy function are

$$
\begin{aligned}
c_1 &= \frac{\mu}{2}\left(\frac{J_m}{J_m - I_1 + 3}\right), \\
c_3 &= k_1 J_f \left(\frac{(I_4 - 1)}{J_f - (I_4 - 1)^2}\right), \\
c_5 &= k_1 J_f \left(\frac{(I_6 - 1)}{J_f - (I_6 - 1)^2}\right).
\end{aligned}
\tag{3.18}
$$

3.2 Fiber dispersion based models

Fiber dispersion-based models utilize a probability distribution function to model the histological structure of tissues. The models which have angular integration approach and generalized structure tensor approach are outlined in this section.

3.2.1 Driessen-Bouten-Baaijens (DBB) model

Driessen et al. [22] presented an extented version of model of Holzapfel et al. [34] with a fiber volume fraction. They applied the rule of mixtures and express the isochoric Kirchhoff stress for multiple fiber direction as follows

$$
\tau = \hat{\tau} + \sum_{i=1}^{N} \phi_f^i (\tau_f^i - \mathbf{t}.\hat{\tau}.\mathbf{t})\mathbf{t} \otimes \mathbf{t} \tag{3.19}
$$

where $\hat{\tau}$ is the isotropic matrix stress, ϕ_f^i is the volume fraction of fibers and τ_f^i is the fiber stress. The isotropic matrix material is modelled as Neo-Hookean material with shear modulus G. The stress expressions for the isotropic matrix and fibers are

$$
\hat{\tau} = G(\boldsymbol{b} - \mathbf{1}) \quad \text{and} \quad \tau_f^i = k_1 \bar{\lambda}^2 \left[k_2 \text{exp}\left(\bar{\lambda}^2 - 1\right) - 1\right]. \tag{3.20}
$$

They used normal distribution function for the fiber contents. The distribution function is

$$
\phi_f^i(\Phi^i) = \text{A exp}[\frac{-(\Phi^i - \vartheta)^2}{2\sigma^2}] \tag{3.21}
$$

where ϑ is mean value, σ is standard deviation and A is the normalization constant which defined as

$$
\text{A} = \frac{\phi_{tot}}{\sum_{i=1}^{N} \text{exp}[\frac{-(\Phi^i - \vartheta)^2}{2\sigma^2}]} \tag{3.22}
$$

with ϕ_{tot} is total amount of fibers. The shape of PDF for DBB model is given in Figure 3.1.

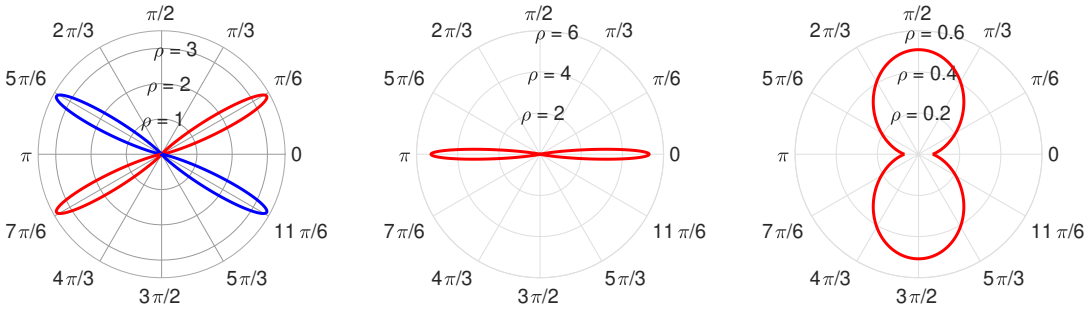

(a) Two families of fibers distribution based on ET dataset for AAA tissue [52].

(b) One family of fibers distribution based on UT dataset for linea alba [14].

(c) One family of fibers distribution based on UT dataset for rectus sheath [50].

Figure 3.1: Polar plots for normal distribution function for DBB model [22].

3.2.2 Gasser-Ogden-Holzapfel (GOH) model

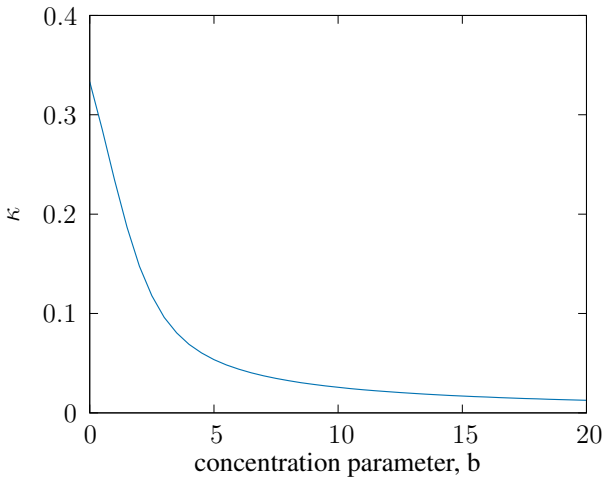

Figure 3.2: Relation between the dispersion parameter κ and the concentration parameter of von Mises distribution.

Gasser et al. [28] assumed that the fibers are distributed rotationally symmetric around a mean direction **M**. They utilized π-periodic von-Mises distribution function. The

von-Mises distribution function is a one-dimensional probability distribution which is a function of Θ and concentration parameter b. The standard von-Mises distribution function is

$$\bar{\rho}(\Theta) = \frac{\exp[b(\cos(2\Theta))}{2\pi I_0(b)} \tag{3.23}$$

where $I_0(b)$ is modified Bessel function of the first kind of order zero according to

$$I_0(b) = \frac{1}{\pi}\int_0^{\pi} \exp(b\cos\Theta)\mathrm{d}\Theta. \tag{3.24}$$

Applying the normalization condsition to 3.23 give the relation

$$I \equiv \int_0^{\pi} \bar{\rho}(\Theta)\mathrm{sin}\Theta\mathrm{d}\Theta \equiv \frac{\exp(-b)}{2\sqrt{2\pi b}}\frac{\mathrm{erfi}(\sqrt{2b}}{I_0(b)}\,. \tag{3.25}$$

Finally, the normalized version of von-Mises distribution is

$$\rho(\Theta) = \bar{\rho}(\Theta)/I = 4\sqrt{\frac{b}{4\pi}}\frac{\exp\left(b\mathrm{cos}(2\Theta)+1\right)}{\mathrm{erfi}\sqrt{2b}} \tag{3.26}$$

By introducing to von-Mises distribution function to 2.28, the generalized structure tensor can be written as

$$\boldsymbol{H} = \kappa\mathbf{1} + (1-3\kappa)\boldsymbol{M}\otimes\boldsymbol{M} \quad \text{with} \quad \kappa = \frac{1}{4}\int_0^{\pi}\rho(\Theta)\sin^3\Theta\mathrm{d}\Theta. \tag{3.27}$$

κ is the intergal measure of fiber dispersion. Figure 3.2 shows a plot of κ as a function of concentration parameter b.

Gasser et al. applied the structure tensor formulation to HGO model. They write the free energy function of anisotropic part

$$\Psi_{fi}(\boldsymbol{C},\boldsymbol{H}_i) = \frac{k_1}{2k_2}[\exp(k_2\bar{E}_i^2)-1]\,, \quad i=1,2 \tag{3.28}$$

where $\bar{E}_i = \mathbf{H}_i : \mathbf{C}-1$. For isotropic part, they utilized classical neo-Hookean model. The nonzero derivatives of ψ are

$$c_1 = \mu\,, \quad \psi_{fi}^{'} = k_1 E_i\mathrm{exp}(k_2 E_i^2)\,. \tag{3.29}$$

The shape of PDF for GOH model is given in Figure 3.3.

3.2.3 Alastrué-Martinez-Doblaré-Menzel (AMDM) model

Alastrue et al. [1] suggested a constitutive model with rotationally symmetric fiber dispersion based on the micro sphere model. They utilized von Mises distribution

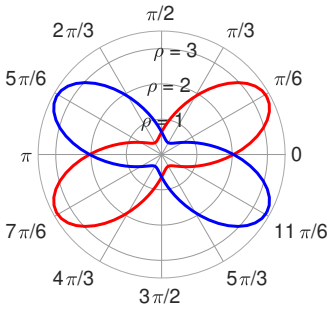

(a) Two families of fibers distribution based ET dataset for AAA tissue [52].

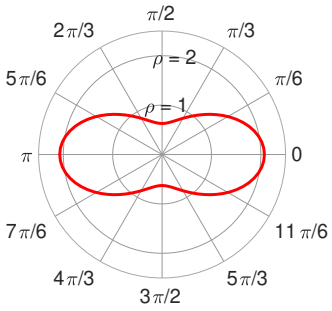

(b) One family of fibers distribution based on UT dataset for linea alba [14].

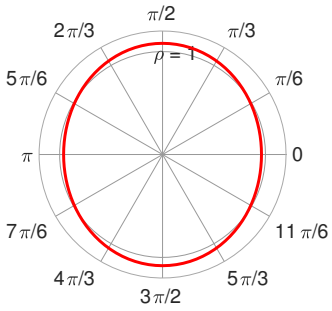

(c) One family of fibers distribution based on UT dataset for rectus sheath [50].

Figure 3.3: Polar plots for von Mises distribution function for GOH model [28].

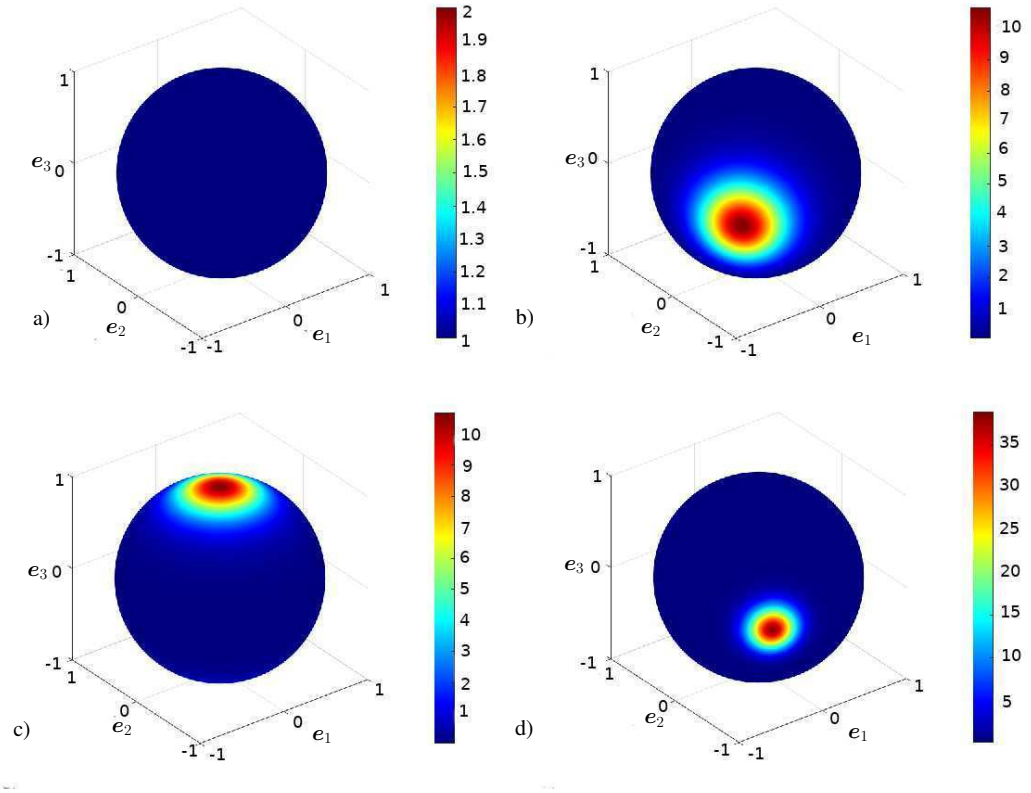

Figure 3.4: Representation of von-Mises distribution function for different parameter set; (a) $b = 0$, $\Theta = 0°$, $\Phi = 0°$ (isotropic case) (b) $b = 3$, $\Theta = 90°$, $\Phi = 45°$, (c) $b = 3$, $\Theta = 0°$, $\Phi = 0°$, (d) $b = 10$, $\Theta = 90°$, $\Phi = 60°$.

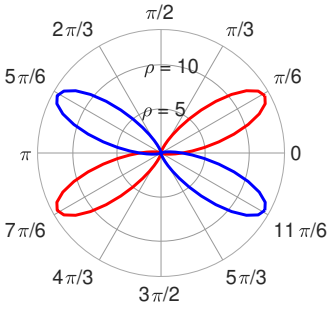

(a) Two families of fibers distribution based on ET dataset for AAA tissue [52].

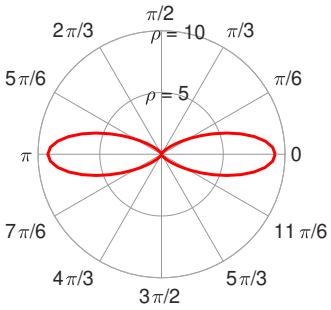

(b) One family of fibers distribution based on UT dataset for linea alba [14].

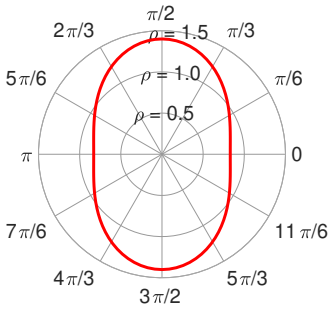

(c) One family of fibers distribution based on UT dataset for rectus sheath [50].

Figure 3.5: Polar plots for von Mises distribution function for AMDM model [1].

function given in 3.26. $\boldsymbol{r}$ is the unit orientation vector of a micro-fiber and $\boldsymbol{t} := \boldsymbol{F}\boldsymbol{r}$ is the Eulerian counterpart of the Lagrengian fiber vector. The affine-stretch of a single fiber in the orientation directiron $\boldsymbol{r}$ reads

$$\bar{\lambda} := \sqrt{\boldsymbol{t}_\flat \cdot \boldsymbol{t}}\,, \quad \text{where} \quad \boldsymbol{t}_\flat := \boldsymbol{g}\boldsymbol{t}\,. \tag{3.30}$$

The macroscopic free energy corresponding to one family of fibers with the mean direction $\boldsymbol{M}$ and with n fibers per unit volume is defined as

$$\Psi_f = \sum_{i=1}^{n} \rho(\boldsymbol{r}^i; \boldsymbol{M})\psi_f^i \tag{3.31}$$

where ψ_f^i is the ith fiber's free energy in the direction of $\boldsymbol{r}^i$. This expression can be expanded in order to account for N mean directions $\boldsymbol{M}_I$ related to different families of fibers as follows

$$\Psi_{ani} = \sum_{I=1}^{N} \psi_f^I. \tag{3.32}$$

For the affine micro-sphere model, macroscopic free energy of a family of fibers is linked to microscopic free energies of individual fibers

$$\Psi_f^I = \left\langle n\rho_I \psi_f(\bar{\lambda}) \right\rangle = \frac{1}{4\pi} \int_\Omega n\rho_I \psi_f(\bar{\lambda}) dA\,. \tag{3.33}$$

The continuous average in 3.33 is approximated by

$$\langle (\bullet) \rangle = \frac{1}{4\pi} \int_\Omega (\bullet) dA \approx \sum_{i=1}^{m} w^i \, (\bullet)^i \tag{3.34}$$

where ${w^i}_{i=1,...,m}$ are weight factors. For isotropic ground matrix, they utilized neo-Hookean free energy function. The anisotropic free energy function is

$$\psi_f^i = \begin{cases} 0, & \text{if } \bar{\lambda_i} < 1 \\ \dfrac{k_1}{2k_2}[\exp(k_2[\bar{\lambda}_i^2 - 1]^2) - 1], & \text{if } \bar{\lambda_i} \geq 1 \ . \end{cases} \tag{3.35}$$

The contribution of each family of fibers to macroscopic isochoric Kirchhoff stresses can be expressed as continuous average including orientation distribution function, namely

$$\tau_f^I = \left\langle n\rho_I \psi_f' \bar{\lambda}^{-1} \boldsymbol{t} \otimes \boldsymbol{t} \right\rangle \tag{3.36}$$

where ψ_f' is the first derivative of ψ_f with respect to $\bar{\lambda}$,

$$n[\psi_f^i]' = 2k_1 \bar{\lambda}_i [\bar{\lambda}_i^2 - 1] exp(k_2[\bar{\lambda}_i^2 - 1]^2) \ . \tag{3.37}$$

The shape of PDF for AMDM model is given in Figure 3.5.

3.2.4 Alastrué-Saéz-Martinez-Doblaré (ASMD) model

As an extension of their previous model, Alastrué al. [3] included Bingham distribution in their constitutive model. This distribution function exhibits andipodal symmetry and is expressed as

$$\rho(\mathbf{r}; \mathbf{Z}, \mathbf{Q}) \frac{\mathrm{d}A}{4\pi} = [F_{0000}(\mathbf{Z})]^{-1} \mathrm{etr}(\mathbf{Z}.\mathbf{Q}^t.\mathbf{r}.\mathbf{r}^t.\mathbf{Q}) \frac{\mathrm{d}A}{4\pi} \tag{3.38}$$

where $\mathrm{etr}(\bullet) \equiv \exp(\mathrm{tr}(\bullet))$, $\mathbf{Z}$ is a diagonal matrix with eigenvalues $[\kappa_1, \kappa_2, \kappa_3]$, $\mathbf{Q}$ is orthogonal orientation matrix such that $\mathbf{A} = \mathbf{Q}.\mathbf{Z}.\mathbf{Q}^T$ and $F_{0000}(\mathbf{Z})$ is defined as

$$F_{0000}(\mathbf{Z}) = [4\pi]^{-1} \int_\Omega (\mathrm{etr}(\mathbf{Z}.\mathbf{r}.\mathbf{r}^t) \mathrm{d}A = {}_1F_1(\frac{1}{2}; \frac{2}{3}; \mathbf{Z}) \tag{3.39}$$

where ${}_1F_1$ is a confluent hypergeometric function of matrix argument. The shape of the distribution is controlled by κ_1, κ_2, and κ_3. In Figure 3.6, the different shape of PDF can be seen on a micro-sphere.

3.2.5 Holzapfel-Niestrawska-Ogden-Reinisch-Schriefl (HNORS) model

Holzapfel et al. [35] take into account in-plane dispersion of fibers based on the observations of Schriefl et al. [60, 61, 62, 63]. Schriefl et al. recorded that the fibers

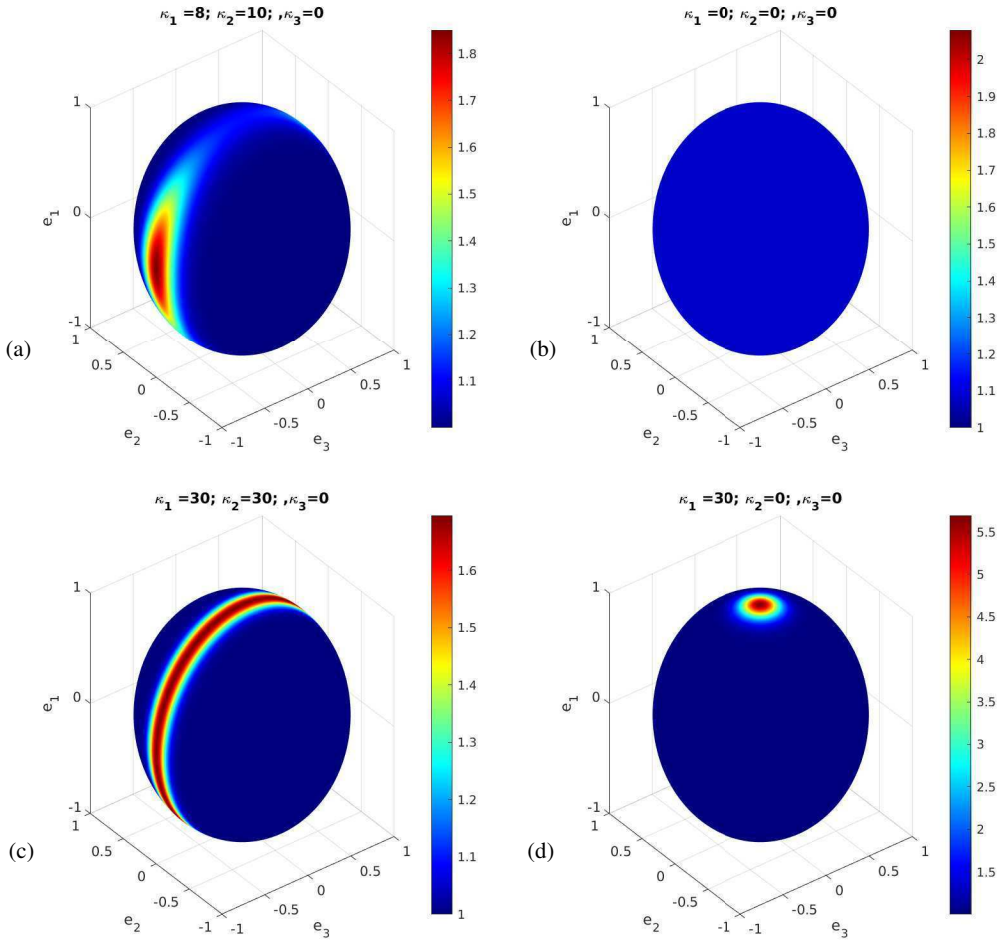

Figure 3.6: Representation of Bingham distribution function for various parameter set showing different shapes of distribution; (a) higher distribution in $\boldsymbol{e}_2$ direction, (b) isotropic case, (c) rotationally symmetric in $\boldsymbol{e}_1 - \boldsymbol{e}_2$ plane, (d) von-Mises distribution with $\boldsymbol{e}_1$ mean direction.

are dispersed both in-plane and out-of-plane, however, they did not observe any correlation between in-plane dispersion and out-of-plane dispersion. Following this evidence, Holzapfel et al. multicatively decomposed the probability density function according to

$$\rho(\boldsymbol{r}) = \rho_{ip}(\Phi)\rho_{op}(\Theta). \tag{3.40}$$

For in-plane distribution, they considered basic von Mises distribution

$$\rho_{ip}(\Theta) = \frac{\exp[a(\cos(2\Theta))}{I_0(a)} \tag{3.41}$$

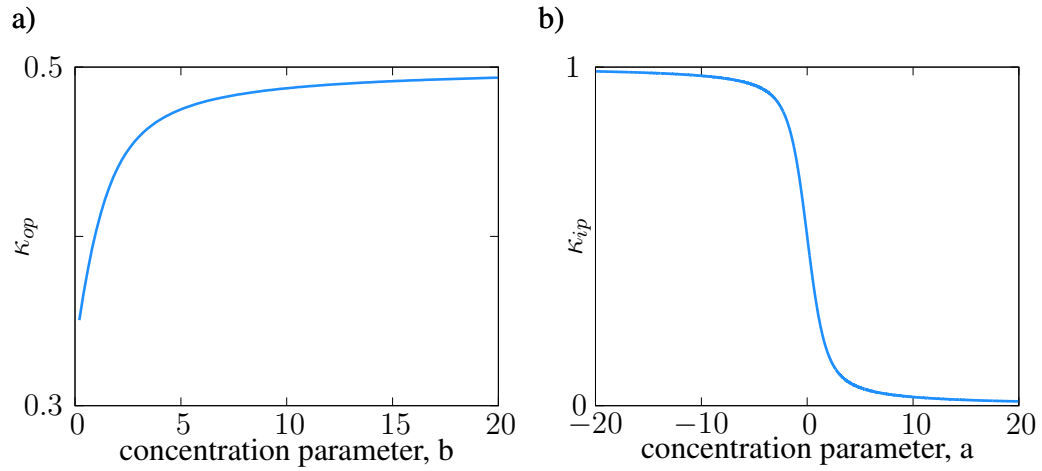

Figure 3.7: a) Relation between the dispersion parameter κ_{op} and the out-of-plane concentration parameter of von Mises distribution,b and b) relation between the dispersion parameter κ_{ip} and the in-plane concentration parameter of von Mises distribution, a .

where a is the concentration parameter and $I_0(a)$ is the modified Bessel function of the first kind of order 0

$$I_0(a) = \frac{1}{\pi}\int_0^{\pi} \exp(x\cos\alpha)d\alpha. \tag{3.42}$$

The out-of-plane distribution is in the form

$$\rho_{op}(\Theta) = 2\sqrt{\frac{2b}{\pi}}\frac{\exp[b(\cos(2\Theta)) - 1]}{erf(\sqrt{2b})}. \tag{3.43}$$

The measures of dispersion in-plane and out-of-plane directions read

$$\kappa_{ip} = \frac{1}{\pi}\int_0^{\pi} \rho_{ip}(\Phi)\sin^2\Phi \mathrm{d}\Phi\,, \quad \kappa_{op} = \int_0^{\pi/2} \rho(\Theta)\sin^3\Theta \mathrm{d}\Theta \tag{3.44}$$

respectively. The structure tensor $\mathbf{H}_4$ and $\mathbf{H}_6$ has the form

$$\mathbf{H}_i = A\mathbf{1} + B\mathbf{M}_i \otimes \mathbf{M}_i + (1 - 3A - B)\mathbf{M}_n \otimes \mathbf{M}_n\,, \quad i = 4, 6 \tag{3.45}$$

where $\mathbf{M}$ is unit vector in-plane mean fibre direction, $\mathbf{M}_n$ is unit out-of-plane vector, while $A = \kappa_{ip}\kappa_{op}$ and $B = 2\kappa_{op}(1 - 2\kappa_{ip})$.

The free energy formulations are same with the model of Gasser et al. [28] which are 3.28, 3.29. The shape of PDF for HNORS model is given in Figure 3.8.

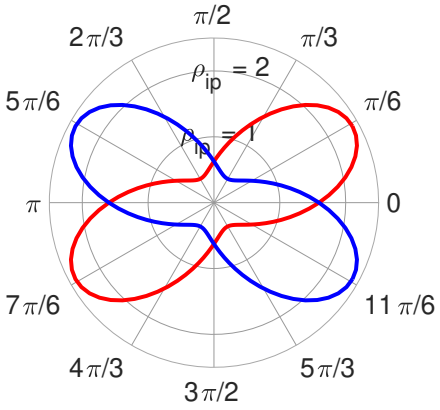

(a) Two families of fibers distribution based on ET dataset for AAA tissue [52].

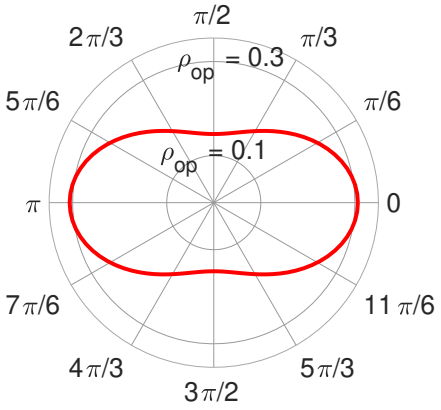

(b) Two families of fibers distribution based on ET dataset for AAA tissue [52].

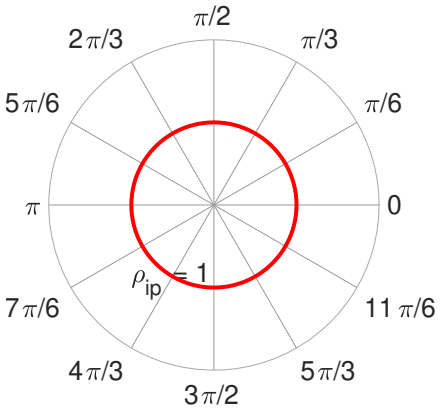

(c) One family of fibers distribution based on UT dataset for linea alba [14].

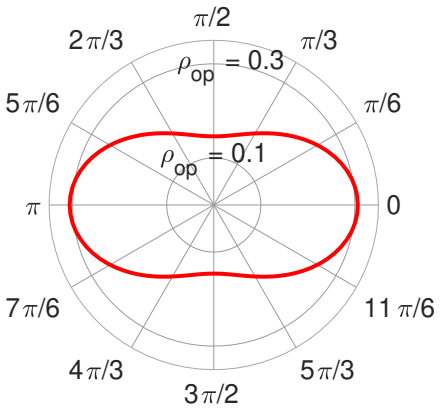

(d) One family of fibers distribution based on UT dataset for linea alba [14].

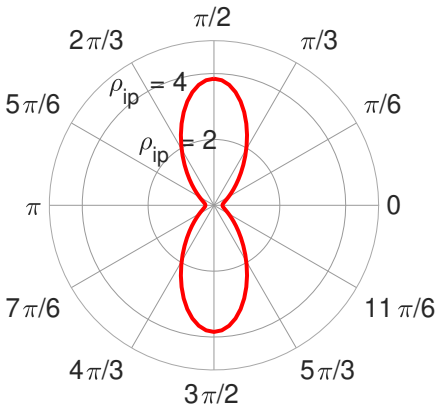

(e) One family of fibers distribution based on UT dataset for rectus sheath [50].

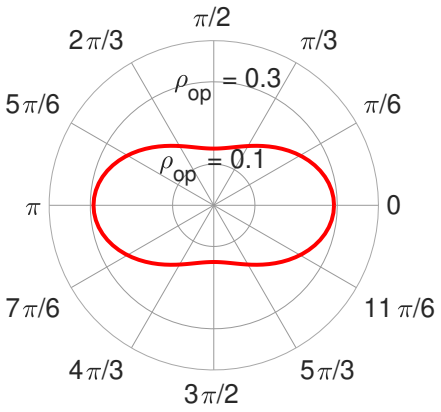

(f) One family of fibers distribution based on UT dataset for rectus sheath [50].

Figure 3.8: Polar plots for bivariate von Mises distribution function for HNORS model [35].

CHAPTER 4

PARAMETER OPTIMIZATION AND COMPARISON OF MODELS

4.1 Parameter optimization

The parameter optimization procedure introduced by Dal et al. [17] has been adopted for anisotropic soft tissues. The parameter identification process is conducted based on error expressions for uniaxial tension experiment in $\boldsymbol{e}_1$-direction, uniaxial tension experiment in $\boldsymbol{e}_2$-direction, and equibiaxial tension experiment in $\boldsymbol{e}_1 - \boldsymbol{e}_2$ directions,

$$\boldsymbol{\mathcal{E}}_{UT_1}(\boldsymbol{\zeta}) = \sum_{i=1}^{n_{UT_1}} \left(P_{11}(\boldsymbol{\zeta}, \lambda_i) - P_{11}^{exp}(\lambda_i)\right)^2 , \tag{4.1}$$

$$\boldsymbol{\mathcal{E}}_{UT_2}(\boldsymbol{\zeta}) = \sum_{i=1}^{n_{UT_2}} \left(P_{22}(\boldsymbol{\zeta}, \lambda_i) - P_{22}^{exp}(\lambda_i)\right)^2 , \tag{4.2}$$

$$\boldsymbol{\mathcal{E}}_{ET}(\boldsymbol{\zeta}) = \sum_{i=1}^{n_{ET}} \left(P_{11}(\boldsymbol{\zeta}, \lambda_i) - P_{11}^{exp}(\lambda_i)\right)^2 , \tag{4.3}$$

$$\boldsymbol{\mathcal{E}}_{ET}(\boldsymbol{\zeta}) = \sum_{i=1}^{n_{ET}} \left(P_{22}(\boldsymbol{\zeta}, \lambda_i) - P_{22}^{exp}(\lambda_i)\right)^2 , \tag{4.4}$$

respectively. P_{11} is the fist Piola-Kirchhoff stress. n_{UT_1}, n_{UT_2}, n_{ET} are number of data points for UT in $\boldsymbol{e}_1$, UT in $\boldsymbol{e}_2$, and ET experiments, respectively. The total cost function for UT tests and ET test are

$$\boldsymbol{\mathcal{E}}_{TOT}^{UT}(\boldsymbol{\zeta}, \boldsymbol{w}) = w_1 \boldsymbol{\mathcal{E}}_{UT_1}(\boldsymbol{\zeta}) + w_2 \boldsymbol{\mathcal{E}}_{UT_2}(\boldsymbol{\zeta}) , \tag{4.5}$$

$$\boldsymbol{\mathcal{E}}_{TOT}^{ET}(\boldsymbol{\zeta}, \boldsymbol{w}) = w_1 \boldsymbol{\mathcal{E}}_{ET_1}(\boldsymbol{\zeta}) + w_2 \boldsymbol{\mathcal{E}}_{ET_2}(\boldsymbol{\zeta}) . \tag{4.6}$$

The total cost functions are presented for UT tests and ET tests individually since there is a lack of UT and ET test data that belong exactly the same tissue. The parameters extended with including the weights in 4.6, $\boldsymbol{\xi} := \{\boldsymbol{\zeta}, \boldsymbol{w}\}$ which is obtained

from the minimization principle

$$\boldsymbol{\xi} = \text{Arg}\left\{\inf_{\boldsymbol{\xi}\in\mathcal{W}} \mathcal{E}_{\text{TOT}}(\boldsymbol{\xi})\right\} . \tag{4.7}$$

Following constraint domain is applied to the optimization process,

$$\mathcal{W} = \{\boldsymbol{\zeta} \mid \boldsymbol{\zeta} \in \mathcal{D} \ \wedge \ \boldsymbol{w} \mid w_i \in [0,1]\} , \tag{4.8}$$

with $w_1+w_2 = 1$. The domain $\mathcal{D}$ is the physically meaningful domain for the material parameters ζ. The gradient type optimization is conducted by Fmincon function in Matlab where the extended cost function

$$\mathcal{L}(\boldsymbol{\xi}, \boldsymbol{\lambda}^{\text{eq}}, \boldsymbol{\lambda}^{\text{ine}}) = \mathcal{E}_{\text{TOT}}(\boldsymbol{\xi}) + \sum_i \lambda_i^{\text{ine}} g^i(\boldsymbol{\xi}) + \sum_i \lambda_i^{\text{eq}} h^i(\boldsymbol{\xi}) \tag{4.9}$$

is applied to equality constraints $h^i(\boldsymbol{\xi})$ and inequality constraints $g^i(\boldsymbol{\xi})$, respectively. To obtain an optimum solution, the variation of cost functions with respect to extended parameters requires

$$\nabla_{\boldsymbol{\xi}} \mathcal{L}(\boldsymbol{\xi}, \boldsymbol{\lambda}^{\text{eq}}, \boldsymbol{\lambda}^{\text{ine}}) = \mathbf{0} , \tag{4.10}$$

inclusive of the Karush-Kuhn-Tucker optimality conditions for inequality constraints

$$\lambda_i^{\text{ine}} \geq 0 \qquad g^i(\boldsymbol{\xi}) \leq 0 \qquad \lambda_i^{\text{ine}} g^i(\boldsymbol{\xi}) = 0 , \tag{4.11}$$

where λ_i^{ine} are the Lagrange multipliers for inequality constraint. The penalty parameters λ_i^{eq} enforce the equality constraint,

$$h^i(\boldsymbol{\xi}) = 0 . \tag{4.12}$$

Fmincon function in Matlab

$$\boldsymbol{\xi} = \text{FMINCON}(\mathcal{E}, \boldsymbol{\xi}_0, \boldsymbol{A}, \boldsymbol{b}, \boldsymbol{A}_{\text{eq}}, \boldsymbol{b}_{\text{eq}}) \tag{4.13}$$

is used to minimize $\mathcal{E}$, subject to the linear equality $\boldsymbol{A}_{\text{eq}}\boldsymbol{\xi} = \boldsymbol{b}_{\text{eq}}$ and inequality $\boldsymbol{A}\boldsymbol{\xi} \leq \boldsymbol{b}$. Therein, $\boldsymbol{A}_{\text{eq}}$ is coefficient matrix for equality constraint, $\boldsymbol{b}_{\text{eq}}$ is the vector for equality constraint, $\boldsymbol{A}$ is coefficient matrix for inequality constraints, $\boldsymbol{b}$ is the vector for inequality constraint, and $\boldsymbol{\xi}_0$ are initial points.

4.2 Genetic algorithm

The genetic algorithm introduced by Dal et al. [17] has been adopted in this study. In this section, the genetic algorithm to minimize the error function is outlined.
The genetic algorithm is a search algorithm that utilizes Charles Darwin's theory of natural selection. Analogically, a parameter of a model, a parameter set of a model, and N numbers of possible parameter sets are treated as a gene, a chromosome, and a population of persons with a single chromosome, respectively. Here, our solution is the chromosome. Firstly, the algorithm forms the initial population, and then finds optimal chromosome by operations of mutation, cross-over, and selection.
A gene on a chromosome $A_j = \{a_{1j}, a_{2j}, \ldots, a_{nj}\}$ at location i is denoted by a_{ij}. Therein, n is the number of genes on a chromosome. The models have constraints to have physically meaningful parameters. These constraints are defined over a chromosome for each gene,

$$a_{ij} \in \{c_i \mid c_i \in [\min_i, \max_i]\} \qquad \forall i \in [1, n-2) \tag{4.14}$$

and the constraints on the weights read

$$a_{ij} \in \{w_i \mid w_i \in [0, 1]\} \qquad \forall i \in [n-2, n]. \tag{4.15}$$

Here, the chromosome is the counterpart of the extended parameter set mentioned in 4.1. A decomposition of A_j can be utilized to split these parts as

$$L_j = \{a_{1j}, a_{2j}, \ldots, a_{(n-3)j}\}\ , \quad R_j = \{a_{(n-2)j}, a_{(n-1)j}, a_{nj}\}, \tag{4.16}$$

with $A_j = L_j \cup R_j$. where L_j and R_j represents j^{th} chromosome's material parameters and weights, respectively. The genetic algorithm operates on the same definition of error functions,

$$\begin{aligned} \mathcal{E}_{\text{GA}}(L_j, R_j) &= |R_{1j}|\mathcal{E}_{\text{UT}_1}(L_j) + |R_{2j}|\mathcal{E}_{\text{UT}_2}(L_j) \\ \mathcal{E}_{\text{GA}}(L_j, R_j) &= |R_{1j}|\mathcal{E}_{\text{ET}_1}(L_j) + |R_{2j}|\mathcal{E}_{\text{ET}_2}(L_j) \end{aligned} \tag{4.17}$$

The tuple

$$A_t^* = \min(\{\mathcal{E}_{\text{GA}}(< L_j, R_j >_t), \forall j \in [0, n]\}) \tag{4.18}$$

represents the chromosome at iteration t. The optimal chromosome is found by a stochastic operation known as a mutation, cross-over, and selection. Firstly, the chro-

mosome is mutated with mutation operator, can be expressed as

$$\textsc{Mut}(A_k, s) := \boldsymbol{\alpha}\text{rand}(0,1)a_{sk} + \text{rand}(0,1)(a_{sk} + \boldsymbol{\beta}) \tag{4.19}$$

where, $\boldsymbol{\alpha} := \text{rand}(0, \alpha)$ is mutation amplitude, $\boldsymbol{\beta} := \text{rand}(0, \beta)$ is a severe direct mutation, and $s \in [1, n]$. A chromosome is mutated multiple times with multiple mutation operators,

$$\textsc{Mmut}(A_k, r) := \begin{bmatrix} \textsc{Mut}(A_k, s_1) \\ \textsc{Mut}(A_k, s_1) \\ \cdots \\ \textsc{Mut}(A_k, s_r)\,. \end{bmatrix} \tag{4.20}$$

For a chromosome k, genes are sorted with partitioning operation

$$\begin{aligned} A_{k|m^-} &:= \{a_{1k}, a_{2k}, \ldots, a_{(m-1)k}\}\,, \\ A_{k|m^+} &:= \{a_{mk}, a_{(m+1)k}, \ldots, a_{nk}\}. \end{aligned} \tag{4.21}$$

The chromosome of a person of the population is cross-linked via crossover operator Co is defined as

$$\textsc{Co}(A_k, A_l, m^{\pm}) := \text{cat}(\textsc{Mmut}(\text{perm}(A_k, A_l))) \tag{4.22}$$

where, $\text{cat}(\cdot, \cdot)$ is concatenation of two ordered lists, $\text{perm}(A_{k|m^{\pm}}, A_{l|m^{\pm}})$ is one of the two possible choromosome, namely $< A_{k|m^+}, A_{l|m^-} >$ and $< A_{k|m^-}, A_{l|m^+} >$. Finally, the optimum chromosome is discovered by the selection operator,

$$\textsc{Sel}(P_t, o) := \text{sort}(\mathcal{E}_{\text{GA}}(P_t))_{|o^-} \tag{4.23}$$

where $P_t = \{A_j^t \mid \forall j \in [1, N]\}$ is population at iteration t, and o represent the percentage of surviving chromosomal crossover in the population for the next iteration. The optimum chromosome is selected by taking the first percent o of the chromosome crossing based on the error values in ascending order.

4.3 Comparison of hyperelastic models

The quality of fit metric (χ^2) is used to compare the fitting performance of models. The quality of fit parameter for a uniaxial dataset of Cooney and Martins is

$$\begin{aligned}\chi^2 = & \sum_{i=1}^{n_{UT_1}} \frac{\left(P_{11}^{UT_1}(\lambda_i) - P_{11}^{exp,UT_1}(\lambda_i)\right)^2}{P_{11}^{exp,UT_1}(\lambda_i)} \\ + & \sum_{i=1}^{n_{UT_2}} \frac{\left(P_{22}^{UT_2}(\lambda_i) - P_{22}^{exp,UT_2}(\lambda_i)\right)^2}{P_{22}^{exp,UT_2}(\lambda_i)},\end{aligned} \tag{4.24}$$

where n_{UT_1} and n_{UT_2} are the number of data points and $P_{11}^{UT_1}$ and $P_{22}^{UT_2}$ are the first and the second Piola-Kirchhoff stresses for UT test in $\boldsymbol{e}_1$ and UT test in $\boldsymbol{e}_2$ directions. Similarly, for the equibiaxial loading case, the quality of fit parameter for fitting dataset of Niestrawska is

$$\begin{aligned}\chi^2 = & \sum_{i=1}^{n_{ET_1}} \frac{\left(P_{11}^{ET}(\lambda_i) - P_{11}^{exp,ET_1}(\lambda_i)\right)^2}{P_{11}^{exp,ET_1}(\lambda_i)} \\ + & \sum_{i=1}^{n_{ET}} \frac{\left(P_{22}^{ET_2}(\lambda_i) - P_{22}^{exp,ET_2}(\lambda_i)\right)^2}{P_{22}^{exp,ET_2}(\lambda_i)},\end{aligned} \tag{4.25}$$

where n_{ET_1} and n_{ET_2} are the number of data points and $P_{11}^{ET_1}$ and $P_{22}^{ET_2}$ are the first and the second Piola-Kirchhoff stresses for ET test in $\boldsymbol{e}_1 - \boldsymbol{e}_2$ directions.

The quality of fit metric of each model has been presented in three regions based on the stretch ranges,

$$\begin{aligned}\text{region}_1 := & \quad \lambda \in [1, 1/3\lambda_{max}], \\ \text{region}_2 := & \quad \lambda \in [1, 2/3\lambda_{max}], \\ \text{region}_3 := & \quad \lambda \in [1, \lambda_{max}]\,.\end{aligned} \tag{4.26}$$

CHAPTER 5

RESULTS AND CONCLUSION

In this section, we will discuss the performance of the 9 hyperelastic models reviewed in Chapter 3. The procedure for the parameter identification is outlined in Chapter 4.

5.1 Results and discussion

Table 5.1: Models sorted based on the *quality of fit* to ET dataset for AAA tissue [52]

simultaneous fit sorting results for ET dataset			
rank	**model name**	χ^2	nop
1	HNORS model [35]	2.4368	6
2	HSGR model [39]	2.4734	5
3	AMDM model [1]	2.8541	5
4	GOH model [28]	3.3643	5
5	ASMD model [3]	3.7984	6
6	NY model [51]	11.0814	4
7	DBB model [22]	30.5514	6
8	HGO model [34]	47.4992	4
9	OS model [53]	86.1323	5

The models are compared based on their quality of fit metric using ET dataset for AAA tissue [52], UT dataset for linea alba [14], and UT dataset for rectus sheath [50]. Figures 5.1–5.9 represent simultaneous fit results of models to ET dataset for AAA tissue [52], UT dataset for linea alba [14], and UT dataset for rectus sheath [50]. In the parameter optimization procedure, we have adherent to histological informa-

Table 5.2: Models sorted based on the *quality of fit* to UT dataset for linea alba [14]

simultaneous fit sorting results for UT dataset			
rank	**model name**	χ^2	nop
1	GOH model [28]	0.7905	5
2	HSGR [39]	0.8311	5
3	AMDM model [1]	0.9163	5
4	HNORS model [35]	0.9711	6
5	OS model [53]	1.1294	5
6	ASMD model [3]	1.2527	6
7	HGO model [34]	1.2529	4
8	NY model [51]	11.3349	4
9	DBB model [22]	19.6485	6

Table 5.3: Models sorted based on the *quality of fit* to UT dataset for rectus sheath [50]

simultaneous fit sorting results for UT dataset			
rank	**model name**	χ^2	nop
1	NY model [51]	0.0949	4
2	GOH model [28]	0.4049	5
3	HNORS model [35]	0.4492	6
4	HSGR model [39]	0.5021	5
5	AMDM model [1]	0.5563	5
6	ASMD model [3]	0.6011	6
7	DBB model [22]	2.4414	6
8	HGO model [34]	3.2678	4
9	OS model [53]	3.3823	5

tion provided by Niestrawska et al. [52], Cooney et al. [14], and Martins et al. [50]; for each model, we have imposed the same fiber directions. However, because of the lack of distributed data, we decided to treat distribution parameters as model parameters, and we have obtained them from the optimization procedure. In the ideal

case, the distribution parameters should have been obtained by fitting the probability distribution function to the distribution data of fibers.

Using ET dataset for AAA tissue [52], the models are sorted regarding the quality of fit metric, and results are listed in Table 5.1. ET dataset for AAA tissue was obtained from an arterial wall specimen with two families of fibers. The first 5 models showed the remarkable fitting performance to ET dataset of AAA tissue [1, 3, 28, 35, 39]. The common point of these models is taking into account the fiber dispersion. In these models, except HSGR model [39], the histological structure of tissues is represented by a probability distribution function. HSGR model [39] uses a phenomenological parameter to represent a measure of dispersion, however, since the limits of this parameter are well defined, it is easy to identify. The best model according to fitting performance to ET dataset of AAA tissue is the HNORS model [35] with 6 parameters. The HNORS model is the only model that considers the out-of-plane distribution of fibers. The best model with 5 parameters is the HSGR model, and with 4 parameters is the NY model [51]. AMDM model [1] and GOH model [28] also showed excellent fitting performance; these two models consider fiber dispersion with the same von-Mises distribution function and uses equivalent free energy function. The only difference between these models is the formulation approach. AMDM model [1] uses the angular integration approach, while GOH model [28] uses the generalized structure tensor. Their fitting performance is almost equivalent, however, the computational effort of GOH model [28] is significantly low compared to AMDM model [1]; our observation for the comparison of AI formulation and GST formulation is in line with Holzapfel and Ogden [37].

The comparison result of models based on UT dataset for linea alba is listed in Table 5.2. UT dataset for linea alba does not show highly nonlinear stretch-stress behavior. In line with the comparison on dataset for AAA tissue, fiber dispersion models have better fitting performance on linea alba dataset compare to invariant-based models, however, the HNORS model [35] is not the best model according to fitting performance on linea alba dataset. This is particularly due to the dispersion of fibers of human linea alba; in linea alba, collagen fibers have a less sophisticated distribution than collagen distribution of arterial wall. Thus, using higher-order distribution functions to represent fiber distributions loses importance and increases computational complexity. GOH model [28] has the best fitting performance on linea alba dataset

with 5 parameters.

The quality of fit metrics of each model for dataset of rectus sheath is listed in Table 5.3. It can be observed that in both directions, the stretch-stress response of the rectus sheath tissue is nonlinear. NY model [51] has the best fitting performance on rectus sheath dataset [50]. Besides the other 8 models, the NY model [51] is the only model which does not decompose free energy function into the isotropic part and anisotropic part. Thus, even the experiment data presents stretch-stress information in the transverse direction to the fibers, the NY model [51] considers this data as fibrous data. Therefore, although the NY model [51] does not represent the histological structure accurately, it is able to capture stretch-stress response mathematically. However, the disadvantage of not decomposing free energy function can be seen when the fitting performance of NY model [51] on UT dataset for linea alba. In linea alba dataset [14], the data presented in transverse to fiber direction is almost linear, and the NY model [51] cannot fit this data. The next best 5 models for rectus sheath dataset are fiber dispersion-based models. This is particularly due to the highly dispersed fiber structure of the rectus sheath; even in transverse to the fiber direction, the experimental data shows J-shape response. Transversely isotropic models such as the HGO model cannot capture this mechanical response, since the non-fibrous part of the tissue is modeled by the neo-Hookean model. However, another transversely isotropic model, the OS model [53] is able to show better fitting performance than the HGO model. Similar to the case of the NY model, the performance of the OS model is not due to the accurate representation of the histological structure of the tissue. The reason is that OS model uses the Gent model [29] for the non-fibrous part of a tissue, which is a non-linear model.

The discussed invariant-based models in this study do not contain I_2 term. I_2 term represent areal stretch and accurate identification of parameters related with I_2 term requires ET experiment. Since, in general, datasets in literature contains only UT experiment, excluding I_2 term is a good option from the parameter identification aspect. All in all, the comparison results demonstrate that fiber dispersion-based models are superior fitting performance over the strain invariant-based models. Since the fiber dispersion-based models are capable to represent the histological structure of different types of tissues, fiber dispersion models can be used in a more generic way to model soft tissues.

5.2 Concluding remarks

In this thesis, material parameters of 9 anisotropic hyperelastic models have been optimized for equibiaxial tension data of an arterial wall, uniaxial tension data of human linea alba, and uniaxial tension data of human rectus sheath. A hybrid genetic algorithm-gradient type optimization technique have been utilized to obtain parameters of each model. Fitting performance of each model have been compared according to their quality of fit metric.

A brief literature study have been given in Chapter 1. In Chapter 2, the basis of continuum mechanics and preliminary derivations for hyperelastic response of biological soft tissue under different loading conditions has been expressed. In Chapter 3, 9 anisotropic hyperelastic constitutive models have been investigated by considering two categories, (i) strain-invariant based models, and (ii) fiber-dispersion based models. Experimental studies in literature is outlined in Chapter 1.2.1; the type of the data selected to be used in this study is given in this section. In Chapter 4, parameter identification procedure and genetic algorithm is presented. Multi-objective functions have been compounded in a single objective function by considering weights and minimized. Fitting performance result of models have been considered in Chapter 5. Plots for ET data of AAA tissue [52], UT data of linea alba [14], and UT data of rectus sheath [50] have been presented.

Overall, it would appear that fiber-dispersion based models have superior performance compare to strain-invariant based models. Although, GST formulation and AI formulation have shown similar performance to represent mechanical response of biological soft tissues, since any numerical intergration is not needed for GST formulation, GST formulation has higher computational efficiency. The present findings confirm that von-Mises PDF describe the dispersion of fibers of soft tissue succesfully.

As a future work, polyconvecity requirements can be imposed to the parameter optimization procedure in order to enhance the optimization algorithm. If a data set with different types of experiments, for instance, UT and ET for the same tissue become available, a simultaneous fit can be performed on this data set; this leads to conduct a more extensive comparison of constitutive models. Further that, the prediction capability of models for ET test data can be investigated using identified parameters by

fitting UT data.

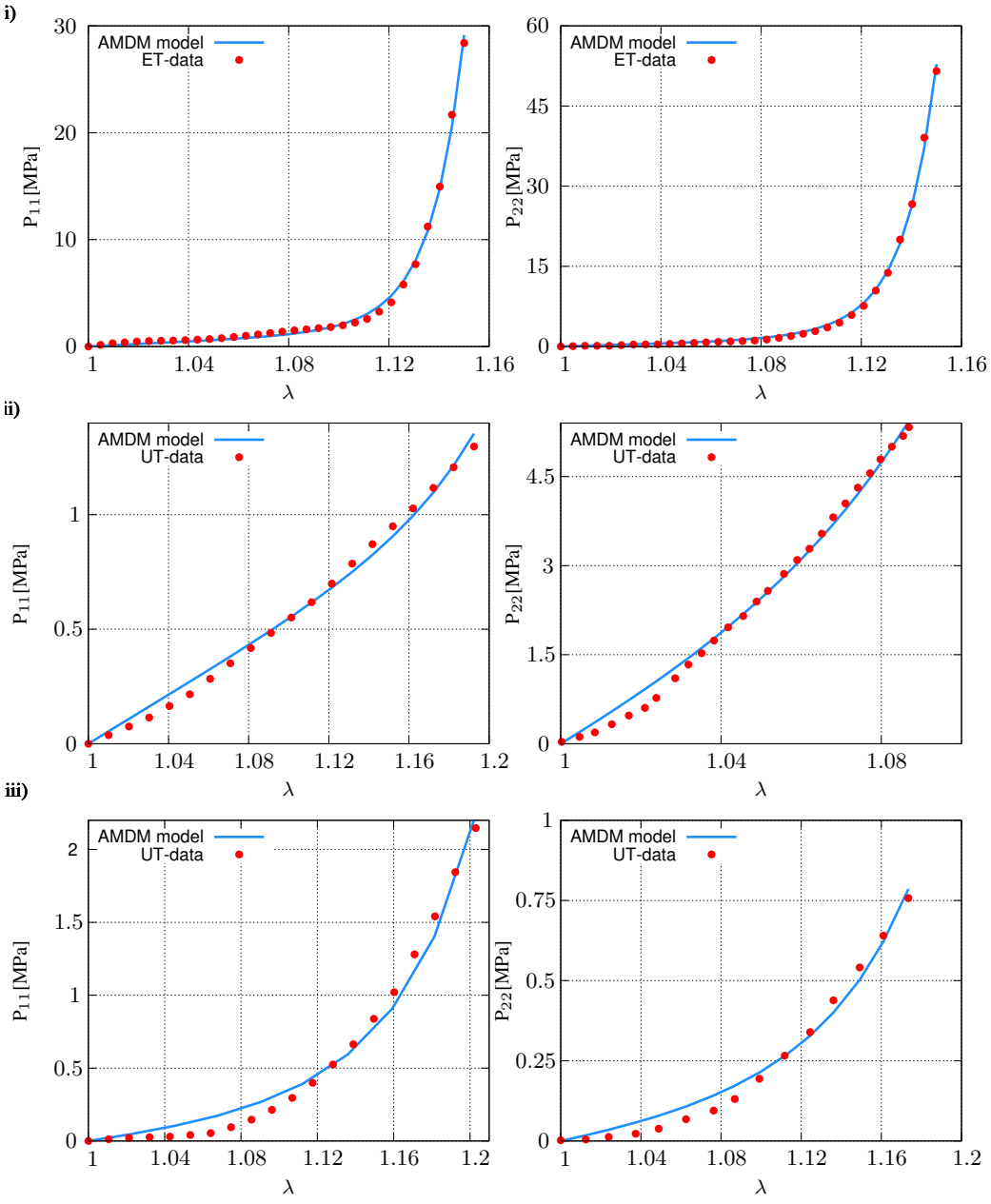

Figure 5.1: AMDM model's [1] predictions for i) ET dataset for AAA tissue [52], ii) UT dataset for linea alba [14], iii) UT dataset for rectus sheath [50].

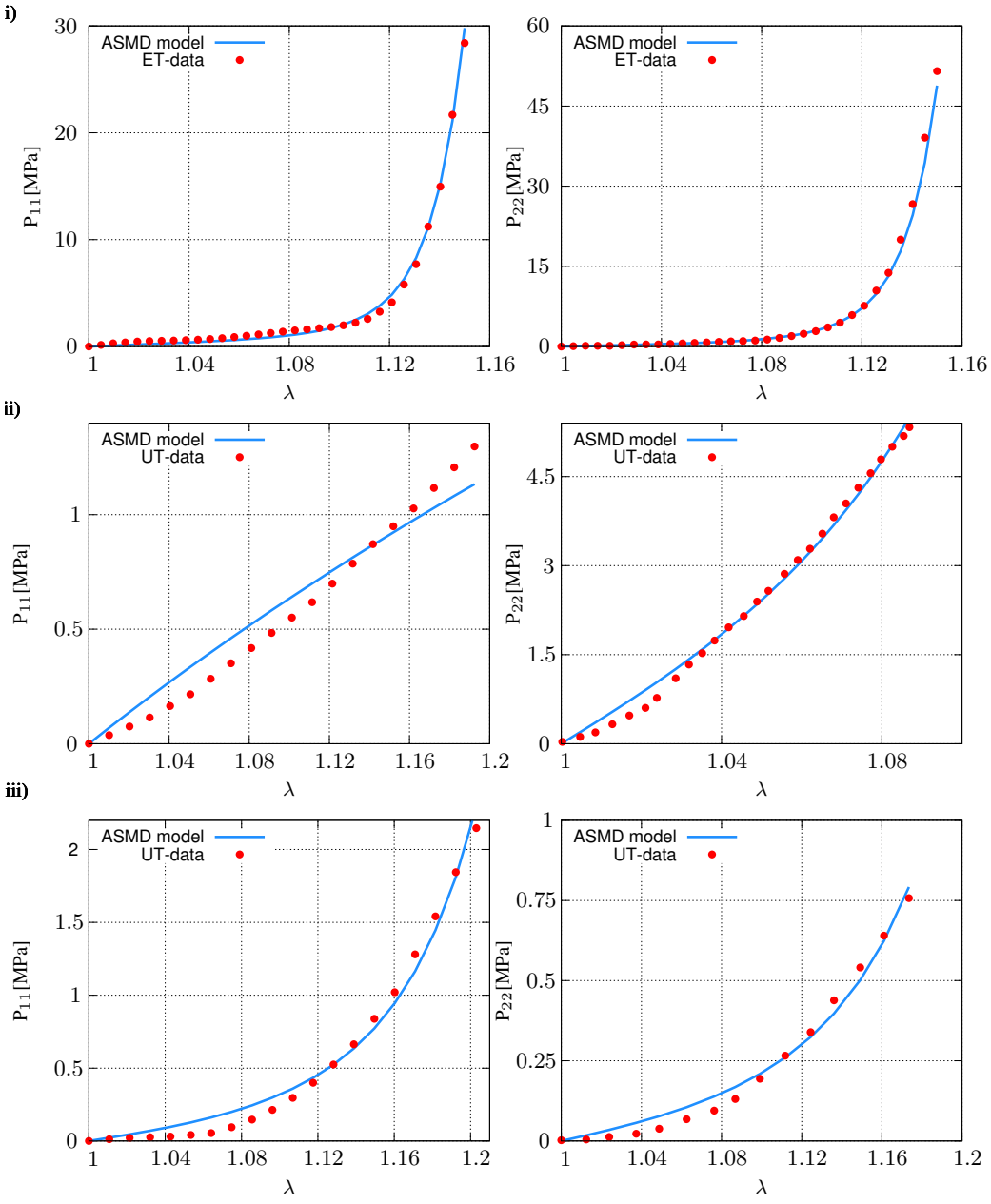

Figure 5.2: ASMD model's [3] predictions for i) ET dataset for AAA tissue [52], ii) UT dataset for linea alba [14], iii) UT dataset for rectus sheath [50].

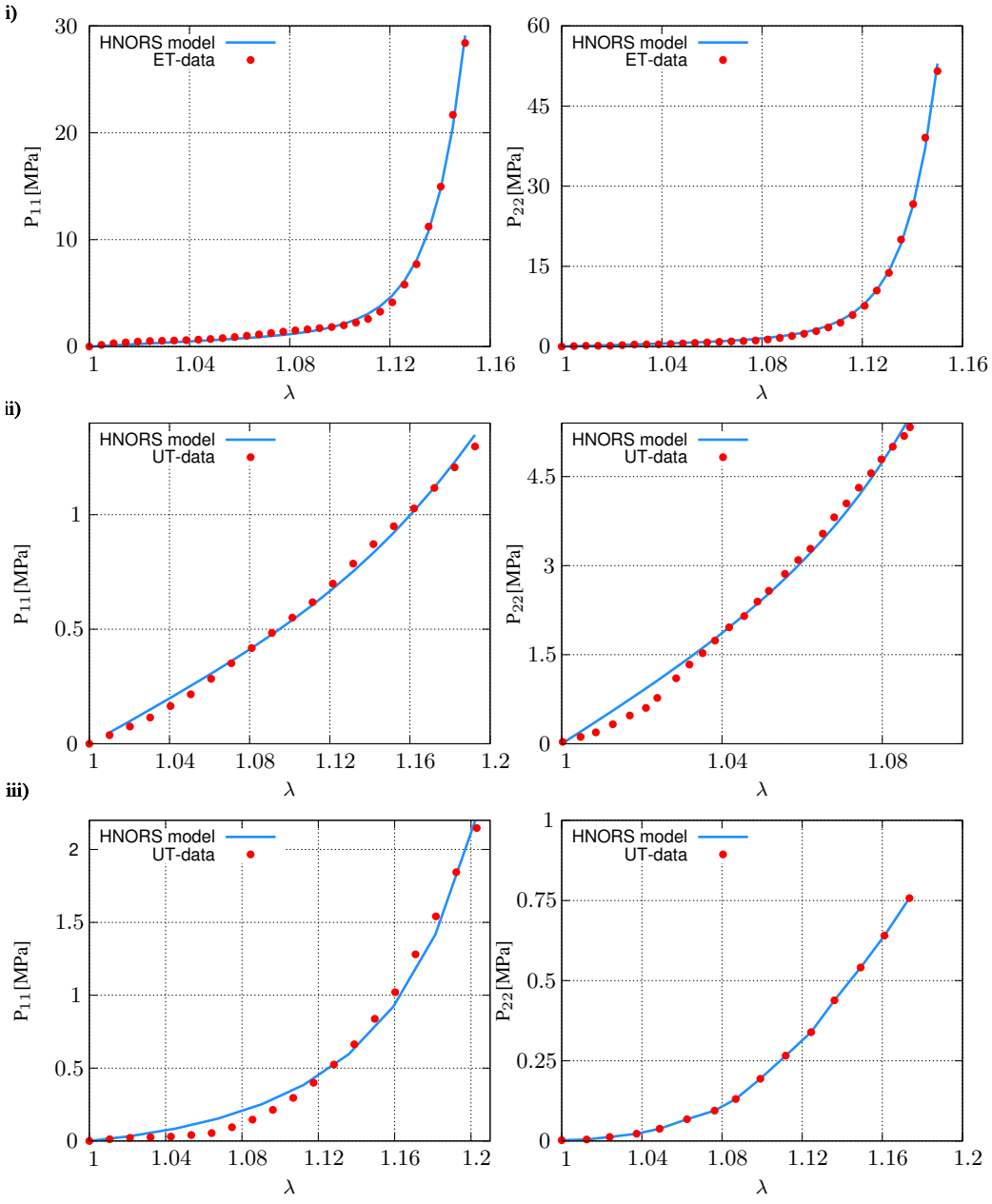

Figure 5.3: HNORS model's [35] predictions for i) ET dataset for AAA tissue [52], ii) UT dataset for linea alba [14], iii) UT dataset for rectus sheath [50].

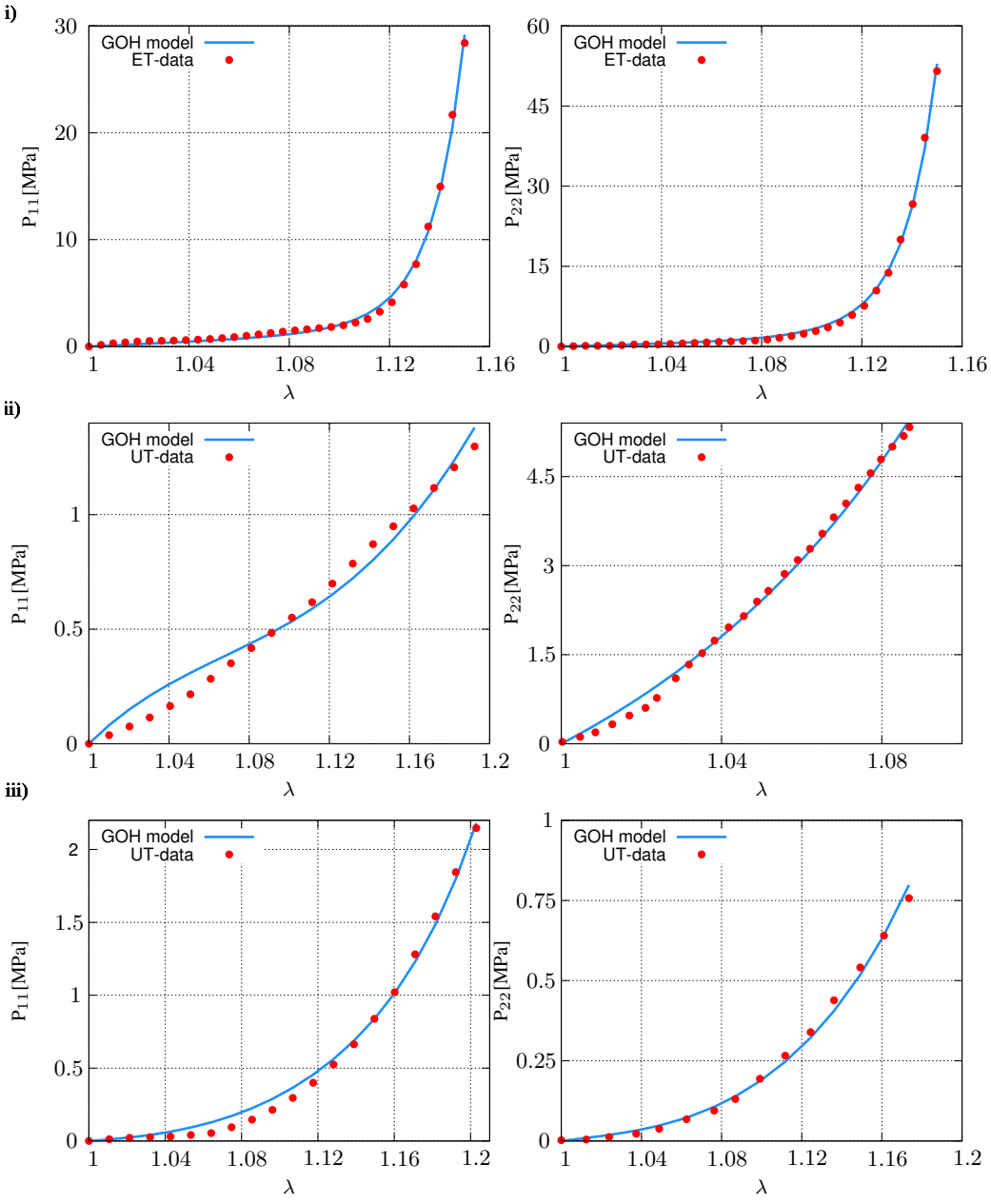

Figure 5.4: GOH model's [28] predictions for i) ET dataset for AAA tissue [52], ii) UT dataset for linea alba [14], iii) UT dataset for rectus sheath [50].

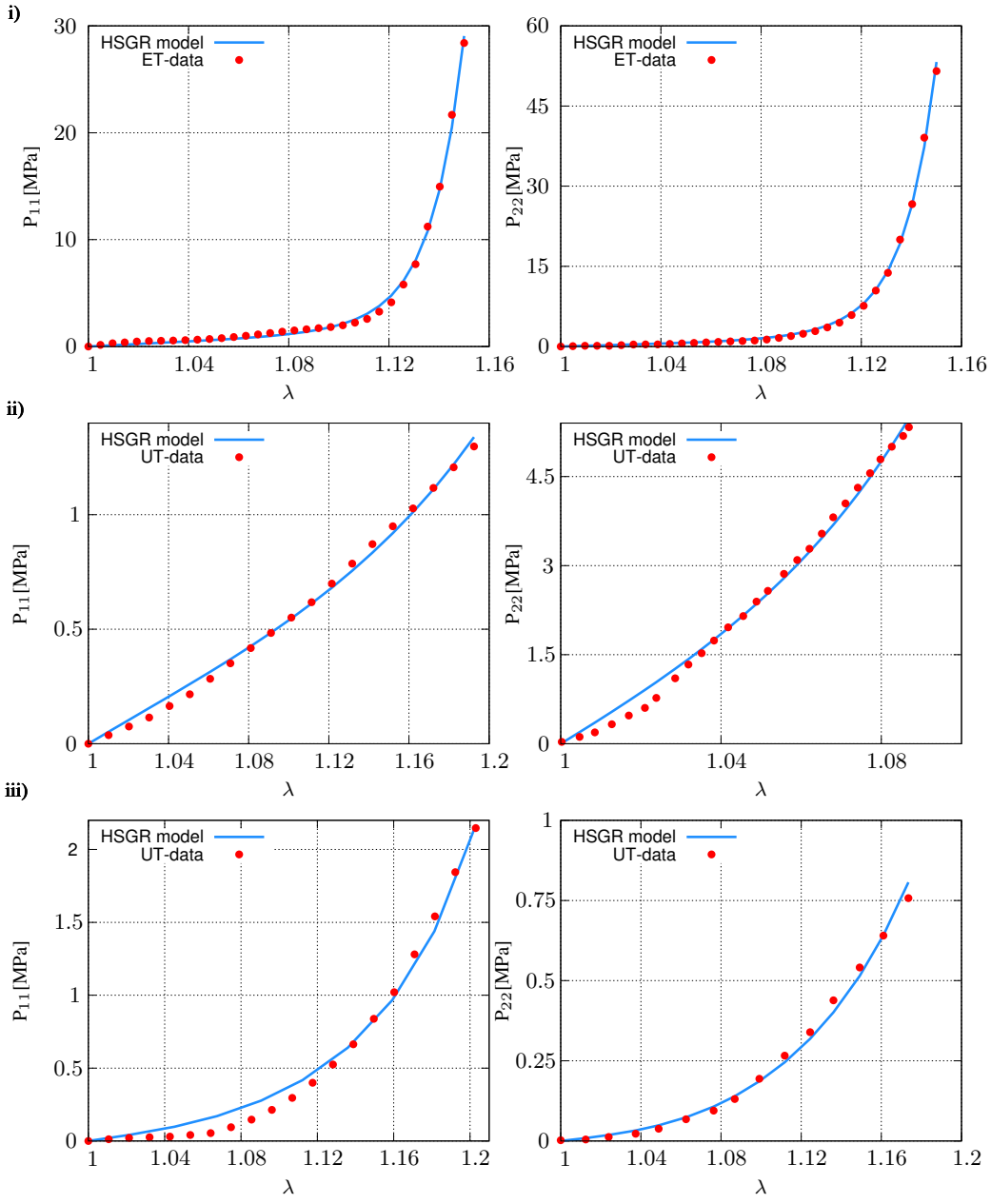

Figure 5.5: HSGR model's [39] predictions for i) ET dataset for AAA tissue [52], ii) UT dataset for linea alba [14], iii) UT dataset for rectus sheath [50].

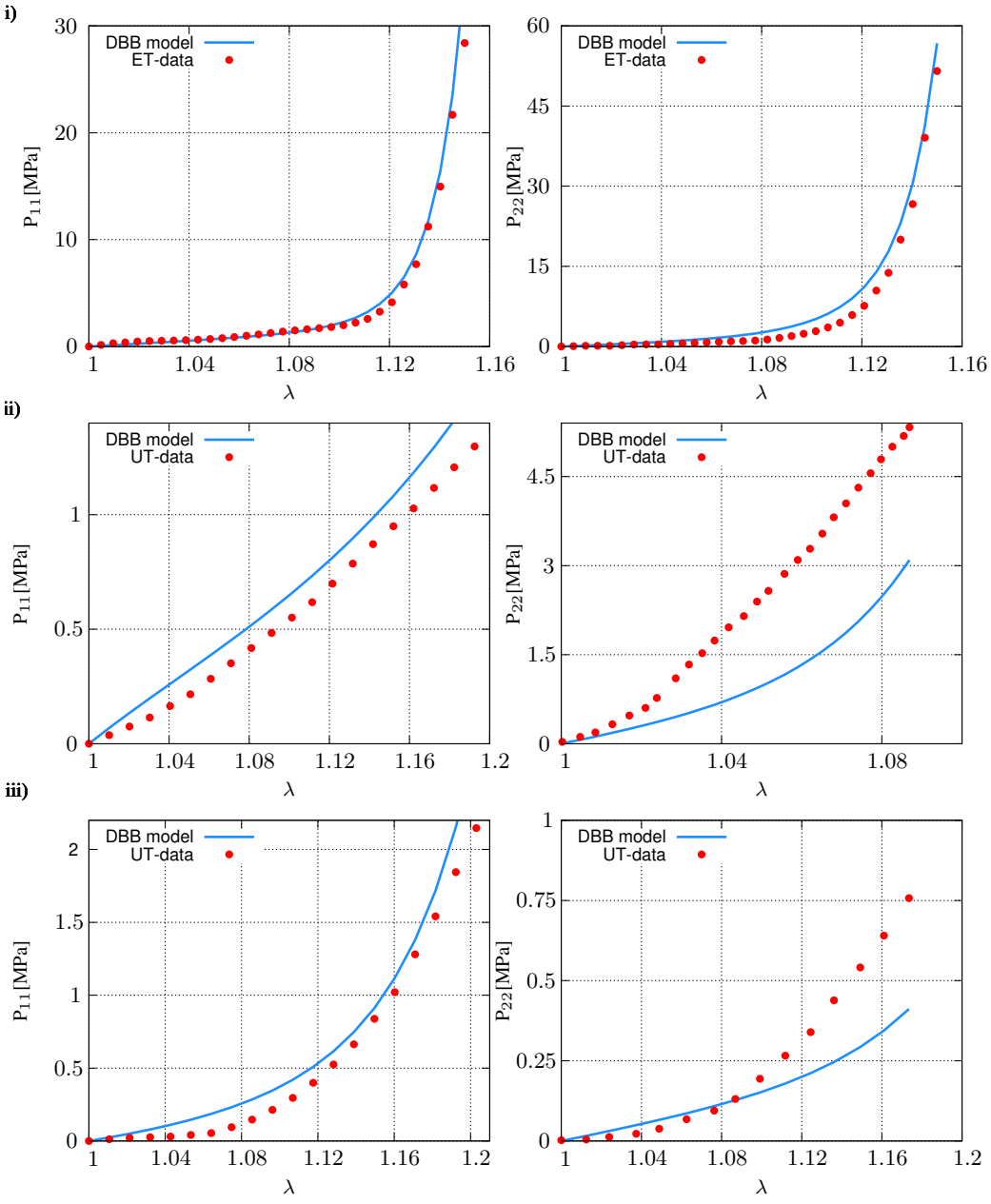

Figure 5.6: DBB model's [22] predictions for i) ET dataset for AAA tissue [52], ii) UT dataset for linea alba [14], iii) UT dataset for rectus sheath [50].

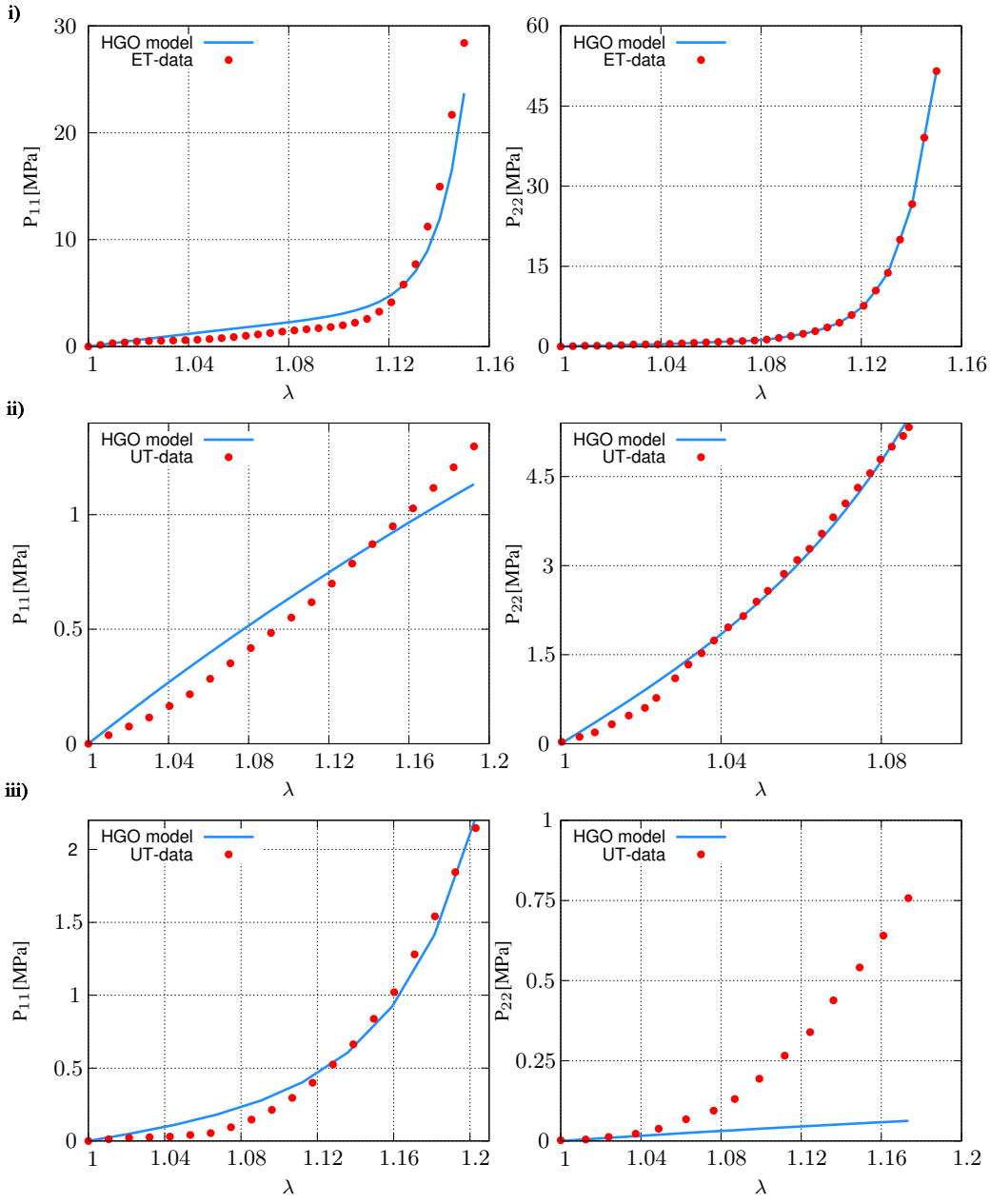

Figure 5.7: HGO model's [34] predictions for i) ET dataset for AAA tissue [52], ii) UT dataset for linea alba [14], iii) UT dataset for rectus sheath [50].

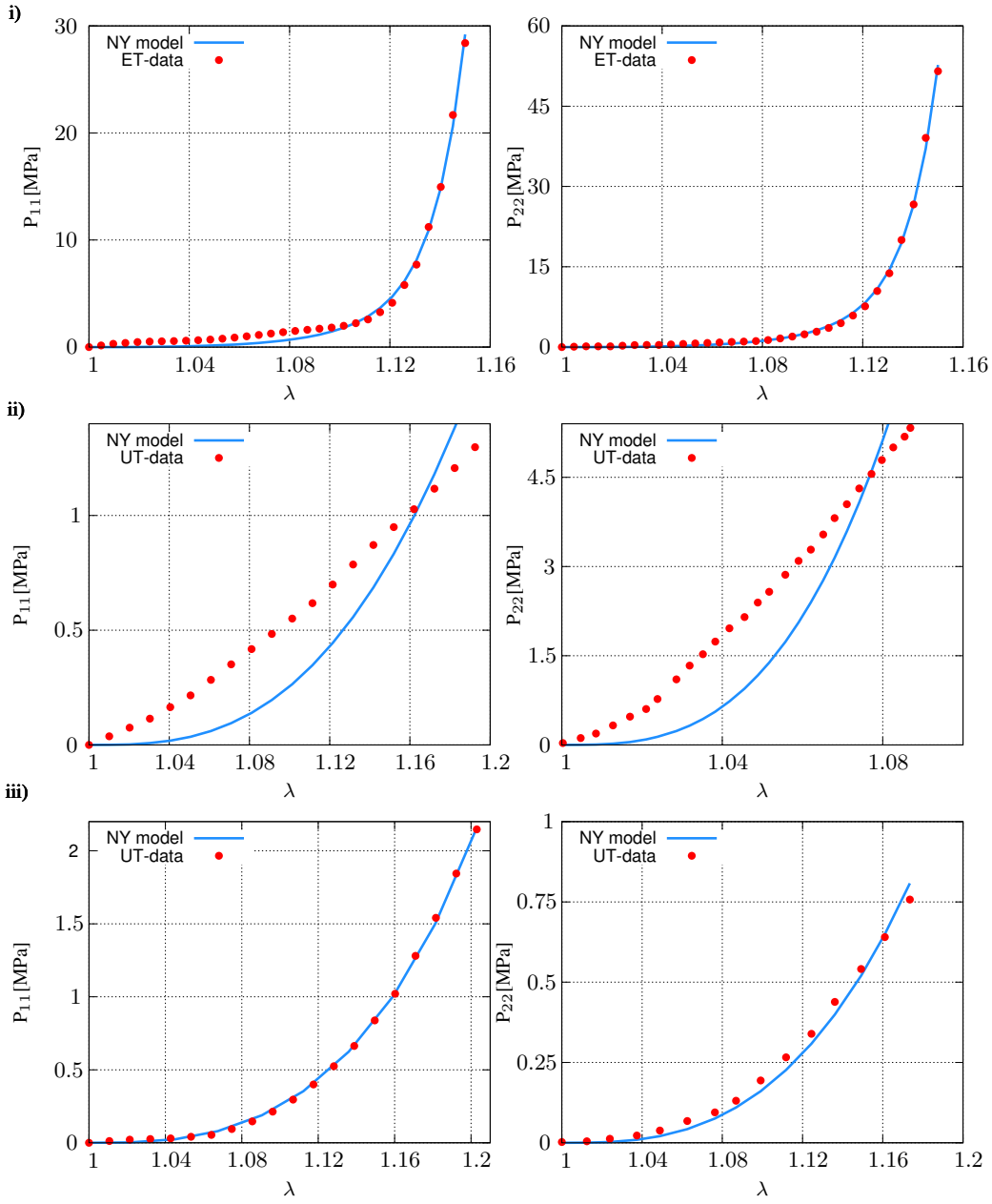

Figure 5.8: NY model's [51] predictions for i) ET dataset for AAA tissue [52], ii) UT dataset for linea alba [14], iii) UT dataset for rectus sheath [50].

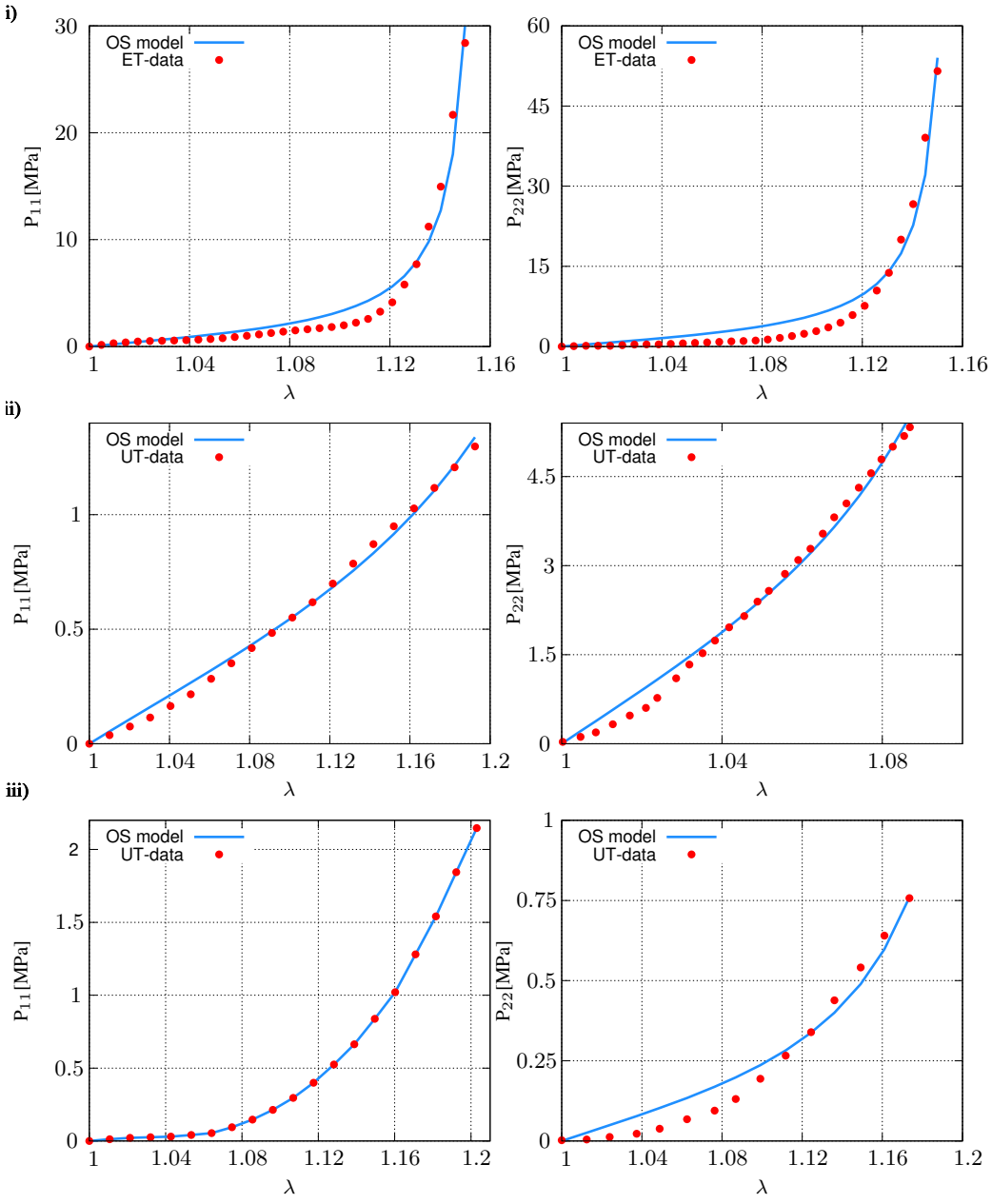

Figure 5.9: OS model's [53] predictions for i) ET dataset for AAA tissue [52], ii) UT dataset for linea alba [14], iii) UT dataset for rectus sheath [50].

REFERENCES

[1] V. Alastrué, M. A. Martínez, M. Doblaré, and A. Menzel. Anisotropic microsphere-based finite elasticity applied to blood vessel modelling. *Journal of the Mechanics and Physics of Solids*, 57(1):178–203, 2009.

[2] V. Alastrué, E. Peña, M. A. Martínez, and M. Doblaré. Experimental study and constitutive modelling of the passive mechanical properties of the ovine infrarenal vena cava tissue. *Journal of Biomechanics*, 41(14):3038–3045, 2008.

[3] V. Alastrué, P. Sáez, M. A. Martínez, and M. Doblaré. On the use of the Bingham statistical distribution in microsphere-based constitutive models for arterial tissue. *Mechanics Research Communications*, 37(8):700–706, 2010.

[4] P. J. Arnoux, P. Chabrand, M. Jean, and J. Bonnoit. A visco-hyperelastic model with damage for the knee ligaments under dynamic constraints. *Computer Methods in Biomechanics and Biomedical Engineering*, 5(2):167–174, 2002.

[5] H. Axer, D. G. V. Keyserlingk, and A. Prescher. Collagen fibers in linea alba and rectus sheaths: I. General scheme and morphological aspects. *Journal of Surgical Research*, 96(1):127–134, 2001.

[6] S. Baek, R. L. Gleason, K. R. Rajagopal, and J. D. Humphrey. Theory of small on large: Potential utility in computations of fluid-solid interactions in arteries. *Computer Methods in Applied Mechanics and Engineering*, 196(31-32):3070–3078, 2007.

[7] K. L. Billiar and M. S. Sacks. Biaxial mechanical properties of the natural and glutaraldehyde treated aortic valve cusp - Part I: Experimental results. *Journal of Biomechanical Engineering*, 122(1):23–30, 2000.

[8] P. B. Canham, H. M. Finlay, J. G. Dixon, D. R. Boughner, and A. Chen. Measurements from light and polarised light microscopy of human coronary arteries fixed at distending pressure. *Cardiovascular Research*, 23(11):973–982, 1989.

[9] B. Cansız, H. Dal, and M. Kaliske. Computational cardiology: A modified hill model to describe the electro-visco-elasticity of the myocardium. *Computer Methods in Applied Mechanics and Engineering*, 315:434–466, 2017.

[10] F. B. C. Cansız, H. Dal, and M. Kaliske. An orthotropic viscoelastic material model for passive myocardium: theory and algorithmic treatment. *Computer Methods in Biomechanics and Biomedical Engineering*, 18(11):1160–1172, 2015. PMID: 24533658.

[11] G. Chagnon, M. Rebouah, and D. Favier. Hyperelastic Energy Densities for Soft Biological Tissues: A Review. *Journal of Elasticity*, 120(2):129–160, 2015.

[12] H. S. Choi and R. P. Vito. Two-dimensional stress-strain relationship for canine pericardium. *Journal of Biomechanical Engineering*, 112(2):153–159, 1990.

[13] C. J. Chuong and Y. C. Fung. Three–dimensional stress distribution in arteries. *Journal of Biomechanical Engineering*, 105(3):268–274, 1983.

[14] G. M. Cooney, S. P. Lake, D. M. Thompson, R. M. Castile, D. C. Winter, and C. K. Simms. Uniaxial and biaxial tensile stress-stretch response of human linea alba. *Journal of the Mechanical Behavior of Biomedical Materials*, 63:134–140, 2016.

[15] D. H. Cortes, S. P. Lake, J. A. Kadlowec, L. J. Soslowsky, and D. M. Elliott. Characterizing the mechanical contribution of fiber angular distribution in connective tissue: comparison of two modeling approaches. *Biomechanics and modeling in mechanobiology*, 9(5):651–658, 2010.

[16] K. D. Costa, P. J. Hunter, J. S. Wayne, L. K. Waldman, and A. D. Mcculloch. A Three-Dimensional Finite Element IVIethod for Large Elastic Deformations of Ventricular Myocardium : II — Prolate Spheroidal. 118(November 1996):1–9, 2016.

[17] H. Dal, K. Açıkgöz, and Y. Badienia. On the Performance of Isotropic Hyperelastic Constitutive Models for Rubber-Like Materials: A State of the Art Review. *Applied Mechanics Reviews*, 73(2), 2021.

[18] H. Dal, S. Göktepe, M. Kaliske, and E. Kuhl. A fully implicit finite element method for bidomain models of cardiac electromechanics. *Computer Methods in Applied Mechanics and Engineering*, 253:323–336, 2013.

[19] H. Demiray. A note on the elasticity of soft biological tissues. *Journal of Biomechanics*, 5(3):309–311, 1972.

[20] H. Demiray and R. P. Vito. Large deformation analysis of soft biomaterials. *International Journal of Engineering Science*, 14(9):789–793, 1976.

[21] H. Demiray, H. W. Weizsäcker, K. Pascale, and H. A. Erbay. A stress-strain relation for a rat abdominal aorta. *Journal of Biomechanics*, 21(5):369–374, 1988.

[22] N. J. Driessen, C. V. Bouten, and F. P. Baaijens. A structural constitutive model for collagenous cardiovascular tissues incorporating the angular fiber distribution. *Journal of Biomechanical Engineering*, 127(3):494–503, 2005.

[23] S. J. Estermann, S. Förster-Streffleur, L. Hirtler, J. Streicher, D. H. Pahr, and A. Reisinger. Comparison of Thiel preserved, fresh human, and animal liver tissue in terms of mechanical properties. *Annals of anatomy = Anatomischer Anzeiger : official organ of the Anatomische Gesellschaft*, 236:151717, 2021.

[24] S. Federico and T. C. Gasser. Nonlinear elasticity of biological tissues with statistical fibre orientation. *Journal of the Royal Society Interface*, 7(47):955–966, 2010.

[25] Y. C. Fung. Elasticity of soft tissues in simple elongation. *The American journal of physiology*, 213(6):1532–1544, 1967.

[26] Y. C. Fung and S. C. Cowin. Biomechanics: Mechanical Properties of Living Tissues, 2nd ed. *Journal of Applied Mechanics*, 61(4):1007, 1994.

[27] Y. C. Fung, K. Fronek, and P. Patitucci. Pseudoelasticity of arteries and the choice of its mathematical expression. *American Journal of Physiology - Heart and Circulatory Physiology*, 6(5), 1979.

[28] T. C. Gasser, R. W. Ogden, and G. A. Holzapfel. Hyperelastic modelling of

arterial layers with distributed collagen fibre orientations. *Journal of the Royal Society Interface*, 3(6):15–35, 2006.

[29] A. Gent. A new constitutive relation for rubber., 1996.

[30] M. Gordon. The Physics of Rubber Elasticity (Third Edition). L. R. G. Treloar, Clarendon Press, Oxford. 1975 pp. xii + 370. *British Polymer Journal*, 8(1):39, 1976.

[31] M. H. Holmes and V. C. Mow. The nonlinear characteristics of soft gels and hydrated connective tissues in ultrafiltration. *Journal of Biomechanics*, 23(11):1145–1156, 1990.

[32] G. A. Holzapfel. Biomechanics of Soft Tissue. In *The handbook of materials behavior models*, volume 3, pages 1049–1063. 2001.

[33] G. A. Holzapfel. Similarities between soft biological tissues and rubberlike materials. *Constitutive Models for Rubber IV - Proceedings of the 4th European Conference for Constitutive Models for Rubber, ECCMR 2005*, pages 607–617, 2005.

[34] G. A. Holzapfel, T. C. Gasser, and R. W. Ogden. A new constitutive framework for arterial wall mechanics and a comparative study of material models. *Journal of Elasticity*, 61(1-3):1–48, 2000.

[35] G. A. Holzapfel, J. A. Niestrawska, R. W. Ogden, A. J. Reinisch, and A. J. Schriefl. Modelling non-symmetric collagen fibre dispersion in arterial walls. *Journal of the Royal Society, Interface*, 12(106), 2015.

[36] G. A. Holzapfel and R. W. Ogden. On the tension-compression switch in soft fibrous solids. *European Journal of Mechanics, A/Solids*, 49:561–569, 2015.

[37] G. A. Holzapfel and R. W. Ogden. Comparison of two model frameworks for fiber dispersion in the elasticity of soft biological tissues. *European Journal of Mechanics, A/Solids*, 66:193–200, 2017.

[38] G. A. Holzapfel, R. W. Ogden, and S. Sherifova. On fibre dispersion modelling of soft biological tissues: A review. *Proceedings of the Royal Society A: Mathematical, Physical and Engineering Sciences*, 475(2224), 2019.

[39] G. A. Holzapfel, G. Sommer, C. T. Gasser, and P. Regitnig. Determination of layer-specific mechanical properties of human coronary arteries with nonatherosclerotic intimal thickening and related constitutive modeling. *American Journal of Physiology - Heart and Circulatory Physiology*, 289(5 58-5):2048–2058, 2005.

[40] G. A. Holzapfel and H. W. Weizsäcker. Biomechanical behavior of the arterial wall and its numerical characterization. *Computers in Biology and Medicine*, 28(4):377–392, 1998.

[41] C. O. Horgan and G. Saccomandi. A new constitutive theory for fiber-reinforced incompressible nonlinearly elastic solids. *Journal of the Mechanics and Physics of Solids*, 53(9):1985–2015, 2005.

[42] J. D. Humphrey. Mechanics of the arterial wall: Review and directions, 1995.

[43] J. D. Humphrey and M. Epstein. Cardiovascular Solid Mechanics: Cells, Tissues, and Organs. *Applied Mechanics Reviews*, 55(5):B103–B104, 2002.

[44] J. D. Humphrey, R. K. Strumpf, and F. C. Yin. Determination of a constitutive relation for passive myocardium: II. -Parameter estimation. *Journal of Biomechanical Engineering*, 112(3):340–346, 1990.

[45] J. D. Humphrey and F. C. Yin. On constitutive relations and finite deformations of passive cardiac tissue: I. A pseudostrain-energy function. *Journal of Biomechanical Engineering*, 109(4):298–304, 1987.

[46] E. Karrer. Kinetic theory of the mechanism of muscular contraction. *Protoplasma*, 18(1):475–489, 1933.

[47] V. A. Kas'yanov and A. I. Rachev. Deformation of blood vessels upon stretching, internal pressure, and torsion. *Mechanics of Composite Materials*, 16(1):76–80, 1980.

[48] Y. Lanir. A structural theory for the homogeneous biaxial stress-strain relationships in flat collagenous tissues. *Journal of Biomechanics*, 12(6):423–436, 1979.

[49] D. H. Lin and F. C. Yin. A multiaxial constitutive law for mammalian left ventricular myocardium in steady-state barium contracture or tetanus. *Journal of Biomechanical Engineering*, 120(4):504–517, 1998.

[50] P. Martins, E. Peña, N. R. Jorge, A. Santos, L. Santos, T. Mascarenhas, and B. Calvo. Mechanical characterization and constitutive modelling of the damage process in rectus sheath. *Journal of the Mechanical Behavior of Biomedical Materials*, 8:111–122, 2012.

[51] K. M. Newman and F. C. Yin. A constitutive law for mitral valve tissue. *Journal of Biomechanical Engineering*, 120(1):38–47, 1998.

[52] J. A. Niestrawska, C. Viertler, P. Regitnig, T. U. Cohnert, G. Sommer, and G. A. Holzapfel. Microstructure and mechanics of healthy and aneurysmatic abdominal aortas: Experimental analysis and modelling. *Journal of the Royal Society Interface*, 13(124), 2016.

[53] R. W. Ogden and G. Saccomandi. Introducing mesoscopic information into constitutive equations for arterial walls. *Biomechanics and Modeling in Mechanobiology*, 6(5):333–344, 2007.

[54] W. A. Osborne, W. Sutherland, and J. N. Langley. The elasticity of rubber balloons and hollow viscera. *Proceedings of the Royal Society of London. Series B, Containing Papers of a Biological Character*, 81(551):485–499, 1909.

[55] A. Pandolfi and M. Vasta. Fiber distributed hyperelastic modeling of biological tissues. *Mechanics of Materials*, 44:151–162, 2012.

[56] T. E. Quan, S. E. Cowper, and R. Bucala. The role of circulating fibrocytes in fibrosis. *Current Rheumatology Reports*, 8(2):145–150, 2006.

[57] M. L. Raghavan and D. A. Vorp. Toward a biomechanical tool to evaluate rupture potential of abdominal aortic aneurysm: Identification of a finite strain constitutive model and evaluation of its applicability. *Journal of Biomechanics*, 33(4):475–482, 2000.

[58] K. Rajagopal, C. Bridges, and K. R. Rajagopal. Towards an understanding of the mechanics underlying aortic dissection. *Biomechanics and Modeling in Mechanobiology*, 6(5):345–359, 2007.

[59] M. S. Sacks. Incorporation of experimentally-derived fiber orientation into a structural constitutive model for planar collagenous tissues. *Journal of Biomechanical Engineering*, 125(2):280–287, 2003.

[60] A. J. Schriefl, M. J. Collins, D. M. Pierce, G. A. Holzapfel, L. E. Niklason, and J. D. Humphrey. Remodeling of intramural thrombus and collagen in an Ang-II infusion ApoE-/-model of dissecting aortic aneurysms. *Thrombosis Research*, 130(3):139–146, 2012.

[61] A. J. Schriefl, A. J. Reinisch, S. Sankaran, D. M. Pierce, and G. A. Holzapfel. Quantitative assessment of collagen fibre orientations from two-dimensional images of soft biological tissues. *Journal of the Royal Society Interface*, 9(76):3081–3093, 2012.

[62] A. J. Schriefl, H. Wolinski, P. Regitnig, S. D. Kohlwein, and G. A. Holzapfel. An automated approach for three-dimensional quantification of fibrillar structures in optically cleared soft biological tissues. *Journal of the Royal Society Interface*, 10(80), 2013.

[63] A. J. Schriefl, G. Zeindlinger, D. M. Pierce, P. Regitnig, and G. A. Holzapfel. Determination of the layer-specific distributed collagen fibre orientations in human thoracic and abdominal aortas and common iliac arteries. *Journal of the Royal Society Interface*, 9(71):1275–1286, 2012.

[64] F. Singh, V. K. Katiyar, and B. P. Singh. A new strain energy function to characterize apple and potato tissues. *Journal of Food Engineering*, 118(2):178–187, 2013.

[65] K. Takamizawa and K. Hayashi. Strain energy density function and uniform strain hypothesis for arterial mechanics, 1987.

[66] D. Tang, C. Yang, S. Kobayashi, J. Zheng, P. K. Woodard, Z. Teng, K. Billiar, R. Bach, and D. N. Ku. 3D MRI-based anisotropic FSI models with cyclic bending for human coronary atherosclerotic plaque mechanical analysis. *Journal of biomechanical engineering*, 131(6):61010, 2009.

[67] P. Tong and Y. C. Fung. The stress-strain relationship for the skin. *Journal of Biomechanics*, 9(10):649–657, 1976.

[68] L. R. G. Treloar. The Elasticity of a Network of Long-Chain Molecules. I. *Rubber Chemistry and Technology*, 16(4):746–751, 1943.

[69] R. N. Vaishnav, J. T. Young, and D. J. Patel. Distribution of stresses and of strain energy density through the wall thickness in a canine aortic segment. *Circulation Research*, 32(5):577–583, 1973.

[70] E. A. Van Dam, S. D. Dams, G. W. Peters, M. C. Rutten, G. W. H. Schurink, J. Buth, and F. N. Van De Vosse. Non-linear viscoelastic behavior of abdominal aortic aneurysm thrombus. *Biomechanics and Modeling in Mechanobiology*, 7(2):127–137, 2008.

[71] J. A. Weiss, B. N. Maker, and S. Govindjee. Finite element implementation of incompressible, transversely isotropic hyperelasticity. *Computer Methods in Applied Mechanics and Engineering*, 135(1-2):107–128, 1996.

[72] M. Zemánek, J. Burša, and M. Děták. Biaxial Tension Tests with Soft Tissues of Arterial Wall. *Engineering Mechanics*, 16(1):3–11, 2009.

[73] M. A. Zulliger, P. Fridez, K. Hayashi, and N. Stergiopulos. A strain energy function for arteries accounting for wall composition and structure. *Journal of Biomechanics*, 37(7):989–1000, 2004.

APPENDIX A

TABLES SUMMARIZING MATERIAL PARAMETERS AND ERROR METRICS BASED ON NIESTRAWSKA'S ET DATA

Table A.1: Identified parameters and error bounds for AMDM model based on AAA tissue dataset

AMDM model [1]					
Simultaneous fitting (AAA tissue dataset)					
Parameters	μ=0.9337 $[MPa]$		k_1=0.9118 $[MPa]$		k_2=46.8474
	φ=28.9°		b=3.67		
			Quality of fit		
	Weight	Error	Region 1	Region 2	Region 3
ET-axial	0.9000	0.1241	0.0000	1.0682	1.4882
ET-circumferential	0.1000	0.2610	0.3232	0.0000	1.3659
Total	1.0000	0.3851	0.3232	1.0682	2.8541

Table A.2: Identified parameters and error bounds for DBB model based on AAA tissue dataset

DBB model[22]					
Simultaneous fitting (AAA tissue dataset)					
Parameters	G=2.0698 $[MPa]$		k_1=6.63 $[MPa]$		k_2=52.9817
	φ=28.9°		σ=0.1173		ϕ_{tot}=0.5
			Quality of fit		
	Weight	Error	Region 1	Region 2	Region 3
ET-axial	0.9000	1.4248	0.0000	0.5705	3.0220
ET-circumferential	0.1000	4.5103	2.3480	0.0000	27.5295
Total	1.0000	5.9351	2.3480	0.5705	30.5514

Table A.3: Identified parameters and error bounds for ASMD model based on AAA tissue dataset

ASMD model[3]					
Simultaneous fitting (AAA tissue dataset)					
Parameters	μ=0.6517 $[MPa]$		k_1=3.5475 $[MPa]$		k_2=46.4817
	κ_1=2.3798$e-07$		κ_2=0.9		κ_3=0
			Quality of fit		
	Weight	Error	Region 1	Region 2	Region 3
ET-axial	0.9000	0.1757	0.0000	1.9907	2.5057
ET-circumferential	0.1000	1.2907	0.0642	0.0000	1.2907
Total	1.0000	2.4010	0.0642	1.9907	3.7984

Table A.4: Identified parameters and error bounds for HNORS model based on AAA tissue dataset

HNORS model [35]					
Simultaneous fitting (AAA tissue dataset)					
Parameters	μ=1.8517 $[MPa]$		k_1=0.6981 $[MPa]$		k_2=59.9093
	κ_{ip}=0.7657		κ_{op}=0.47		φ=28.9°
			Quality of fit		
	Weight	Error	Region 1	Region 2	Region 3
ET-axial	0.1000	0.1249	0	1.0843	1.5269
ET-circumferential	0.9000	0.2429	0.2309	0	0.9099
Total	1.0000	0.3675	0.2309	1.0843	2.4368

Table A.5: Identified parameters and error bounds for GOH model based on AAA tissue dataset

GOH model[28]					
Simultaneous fitting (AAA tissue dataset)					
Parameters	μ=1.7416 $[MPa]$		k_1=4.4460 $[MPa]$		k_2=161.3920 $[MPa]$
	φ=28.9°		κ=0.2256		
			Quality of fit		
	Weight	Error	Region 1	Region 2	Region 3
ET-axial	0.1000	0.1377	0	1.2187	1.6822
ET-circumferential	0.9000	0.3022	0.2795	0	1.6821
Total	1.0000	0.4399	0.2795	1.2187	3.3643

Table A.6: Identified parameters and error bounds for HGO model based on AAA tissue dataset

HGO model [34]					
Simultaneous fitting (AAA tissue dataset)					
Parameters	μ=2.6712 $[MPa]$ k_1=0.1742 $[MPa]$ k_2=55.9001 φ=28.9°				
			Quality of fit		
	Weight	Error	Region 1	Region 2	Region 3
ET-axial	0.1	2.4033	0	7.5929	13.3316
ET-circumferential	0.9000	14.1329	8.7405	0	34.1676
Total	1.0000	16.5362	8.7405	7.5929	47.4992

Table A.7: Identified parameters and error bounds for NY model based on AAA tissue dataset

NY model[51]					
Simultaneous fitting (AAA tissue dataset)					
Parameters	k_0=0.1148 $[MPa]$ k_1=31.1439 k_2=1.5230$e+03$ φ=28.9°				
			Quality of fit		
	Weight	Error	Region 1	Region 2	Region 3
ET-axial	0.1665	0.2941	0	7.7801	8.1602
ET-circumferential	0.8335	0.2693	1.5845	0	2.9212
Total	1.0000	0.5634	1.5845	7.7801	11.0814

Table A.8: Identified parameters and error bounds for HSGR model based on AAA tissue dataset

HSGR model[39]					
Simultaneous fitting (AAA tissue dataset)					
Parameters	μ=0.9347 $[MPa]$ k_1=0.2704 $[MPa]$ k_2=47.0232 φ=28.9° p=0.9126				
			Quality of fit		
	Weight	Error	Region 1	Region 2	Region 3
ET-axial	0.1	0.1255	0	1.0337	1.4823
ET-circumferential	0.9	0.2524	0.2511	1.0337	0.9911
Total	1.0000	0.3779	0.2511	1.0337	2.4734

Table A.9: Identified parameters and error bounds for OS model based on AAA tissue dataset

OS model[53]					
Simultaneous fitting (AAA tissue dataset)					
Parameters	μ=2.5537 $[MPa]$ k_1=3.38107 $[MPa]$ J_h=0.1149 J_m=0.2369 φ=28.9°				
			Quality of fit		
	Weight	Error	Region 1	Region 2	Region 3
ET-axial	0.1	1.3169	0	3.7799	10.4829
ET-circumferential	0.9000	5.7514	16.3691	0	75.6493
Total	1.0000	7.0679	16.3691	3.7799	86.1323

APPENDIX B

TABLES SUMMARIZING MATERIAL PARAMETERS AND ERROR METRICS BASED ON COONEY'S UT DATA

Table B.1: Identified parameters and error bounds for AMDM model based on linea alba dataset

AMDM model [1]					
Simultaneous fitting (linea alba dataset)					
Parameters	μ=0.7418 $[MPa]$		k_1=15.3359 $[MPa]$		k_2=10.6226
	φ=0°		b=2.6374		
			Quality of fit		
	Weight	Error	Region 1	Region 2	Region 3
UT-longitudinal	0.1000	0.0012	0.0800	0.0843	0.0944
UT-transverse	0.9000	0.0170	0.7877	0.8052	0.8219
Total	1.0000	0.0182	0.8677	0.8895	0.9163

Table B.2: Identified parameters and error bounds for ASMD model based on linea alba dataset

ASMD model [3]					
Simultaneous fitting (linea alba dataset)					
Parameters	μ=1.1586 $[MPa]$		k_1=8.6141 $[MPa]$		k_2=11.4239
	κ_1=0.0000		κ_2=26.3508		κ_3=0.0000
			Quality of fit		
	Weight	Error	Region 1	Region 2	Region 3
UT-longitudinal	0.1001	0.0079	0.3336	0.4445	0.4892
UT-transverse	0.8999	0.0171	0.7244	0.7390	0.7635
Total	1.0000	0.0250	1.0580	1.1835	1.2527

Table B.3: Identified parameters and error bounds for GOH model based on linea alba dataset

GOH model [28]					
Simultaneous fitting (linea alba dataset)					
Parameters	μ=2.9048 $[MPa]$		k_1=219.5002 $[MPa]$		k_2=92.8262
	φ=0°		κ=0.2755		
			Quality of fit		
	Weight	Error	Region 1	Region 2	Region 3
UT-longitudinal	0.1000	0.0034	0.3233	0.3352	0.3567
UT-transverse	0.9000	0.0101	0.4103	0.4189	0.4338
Total	1.0000	0.0135	0.7336	0.7541	0.7905

Table B.4: Identified parameters and error bounds for HNORS model based on linea alba dataset

HNORS model [35]					
Simultaneous fitting (linea alba dataset)					
Parameters	μ=0.9455 $[MPa]$		k_1=45.5415 $[MPa]$		k_2=51.1415
	κ_{ip}=0.2260		κ_{op}=0.47		φ=0°
			Quality of fit		
	Weight	Error	Region 1	Region 2	Region 3
UT-longitudinal	0.1000	$6.2653e-04$	0.0378	0.0393	0.0457
UT-transverse	0.9000	0.0214	0.8705	0.8925	0.9254
Total	1.0000	0.0220	0.9083	0.9318	0.9711

Table B.5: Identified parameters and error bounds for HSGR model based on linea alba dataset

HSGR model [39]					
Simultaneous fitting (linea alba dataset)					
Parameters	μ=0.8718 $[MPa]$		k_1=6.3547 $[MPa]$		k_2=14.5184
	φ=0°		p=0.7110		
			Quality of fit		
	Weight	Error	Region 1	Region 2	Region 3
UT-longitudinal	0.1000	$6.8779e-04$	0.0564	0.0580	0.0635
UT-transverse	0.9000	0.0169	0.7309	0.7453	0.7675
Total	1.0000	0.0176	0.7873	0.8033	0.8311

Table B.6: Identified parameters and error bounds for HGO model based on linea alba dataset

HGO model [34]					
Simultaneous fitting (linea alba dataset)					
Parameters	μ=1.1586 $[MPa]$ k_1=8.6064 $[MPa]$ k_2=11.4196 φ=0°				
			Quality of fit		
	Weight	Error	Region 1	Region 2	Region 3
UT-longitudinal	0.1000	0.0079	0.3335	0.4445	0.4892
UT-transverse	0.9000	0.0171	0.7246	0.7392	0.7637
Total	1.0000	0.0250	1.0581	1.1837	1.2529

Table B.7: Identified parameters and error bounds for OS model based on linea alba dataset

OS model[53]					
Simultaneous fitting (linea alba dataset)					
Parameters	μ=1.7592 $[MPa]$ k_1=9.8814 $[MPa]$ J_h=0.2883 J_m=0.0944 φ=0°				
			Quality of fit		
	Weight	Error	Region 1	Region 2	Region 3
UT-longitudinal	0.1000	$8.4265e-04$	0.0709	0.0736	0.0797
UT-transverse	0.9000	0.0245	0.9835	1.0114	1.0496
Total	1.0000	0.0253	1.0544	1.0851	1.1294

Table B.8: Identified parameters and error bounds for NY model based on linea alba dataset

NY model[51]					
Simultaneous fitting (linea alba dataset)					
Parameters	k_0=$2.9076e+03$ $[MPa]$ k_1=0.0028 k_2=0.8380 φ=0°				
			Quality of fit		
	Weight	Error	Region 1	Region 2	Region 3
UT-longitudinal	0.1000	0.0399	0.6616	1.5653	1.7889
UT-transverse	0.9000	0.6957	2.6033	8.3558	9.5460
Total	1.0000	0.7356	3.2648	9.9211	11.3349

Table B.9: Identified parameters and error bounds for DBB model based on linea alba dataset

Driessen et al. model [22]					
Simultaneous fitting (linea alba dataset)					
Parameters	G=0.0310 $[MPa]$		k_1=9.2000 $[MPa]$		k_2=25.5000
	φ=0°		σ=0.0753		ϕ_{tot}=0.5
			Quality of fit		
	Weight	Error	Region 1	Region 2	Region 3
UT-longitudinal	0.5000	0.0155	0.2835	0.4182	0.5979
UT-transverse	0.5000	2.4052	0.9481	8.1202	19.0506
Total	1.0000	2.4207	1.2316	8.5385	19.6485

APPENDIX C

TABLES SUMMARIZING MATERIAL PARAMETERS AND ERROR METRICS BASED ON MARTIN'S UT DATA

Table C.1: Identified parameters and error bounds for AMDM model based on rectus sheath dataset

AMDM model [1]					
Simultaneous fitting (rectus sheath dataset)					
Parameters	μ=$1.8478e-05\ [MPa]$		k_1=$3.1303\ [MPa]$		k_2=9.3118
	φ=90°		b=0.2620		
			Quality of fit		
	Weight	Error	Region 1	Region 2	Region 3
UT-longitudinal	0.9000	0.0065	$.4221$	0.4869	0.5097
UT-transverse	0.1000	$9.1167e-04$	0.1763	0.2386	0.2466
Total	1.0000	$7.41167e-03$	0.5984	0.7254	0.5563

Table C.2: Identified parameters and error bounds for ASMD model based on rectus sheath dataset

ASMD model [3]					
Simultaneous fitting (rectus sheath dataset)					
Parameters	μ=$1.7732e-05\ [MPa]$		k_1=$1.5144\ [MPa]$		k_2=8.2137
	κ_1=9.9874		κ_2=9.4921		κ_3=0
			Quality of fit		
	Weight	Error	Region 1	Region 2	Region 3
UT-longitudinal	0.9000	0.0057	0.7742	0.8907	0.9278
UT-transverse	0.1000	$8.8347e-04$	0.1661	0.2195	0.2289
Total	1.0000	0.0066	0.9403	$0.1.1102$	0.1567

Table C.3: Identified parameters and error bounds for GOH model based on rectus sheath dataset

GOH model [28]					
Simultaneous fitting (rectus sheath dataset)					
Parameters	μ=0.2593 $[MPa]$		k_1=85.3960 $[MPa]$		k_2=202.9680
	φ=90°		κ=0.3277		
			Quality of fit		
	Weight	Error	Region 1	Region 2	Region 3
UT-longitudinal	0.8998	0.0023	0.2770	0.3731	0.3789
UT-transverse	0.1002	$2.9878e-04$	0.0156	0.0195	0.0261
Total	1.0000	0.0026	0.2926	0.3926	0.4049

Table C.4: Identified parameters and error bounds for HNORS model based on rectus sheath dataset

HNORS model [35]					
Simultaneous fitting (rectus sheath dataset)					
Parameters	μ=$1.1528e-04$ $[MPa]$		k_1=18.4005 $[MPa]$		k_2=135.4433
	κ_{ip}=0.5219		κ_{op}=0.39		φ=90°
			Quality of fit		
	Weight	Error	Region 1	Region 2	Region 3
UT-longitudinal	0.8998	0.0047	0.2551	0.3010	0.3186
UT-transverse	0.1002	$5.6306e-04$	0.0769	0.1277	0.1306
Total	1.0000	$5.26306e-03$	0.3321	0.4288	0.4492

Table C.5: Identified parameters and error bounds for HSGR model based on rectus sheath dataset

HSGR model [39]					
Simultaneous fitting (rectus sheath dataset)					
Parameters	μ=0.1317 $[MPa]$		k_1=4.1568 $[MPa]$		k_2=31.8087
	φ=90°		p=0.0553		
			Quality of fit		
	Weight	Error	Region 1	Region 2	Region 3
UT-longitudinal	0.8998	0.0046	0.3804	0.4662	0.4732
UT-transverse	0.1002	$3.9869-04$	0.0153	0.0200	0.0289
Total	1.0000	$4.99869e-03$	0.3957	0.4863	0.5021

Table C.6: Identified parameters and error bounds for HGO model based on rectus sheath dataset

HGO model [34]					
Simultaneous fitting (rectus sheath dataset)					
Parameters	μ=0.0700 $[MPa]$ k_1=0.4498 $[MPa]$ k_2=7.4510 φ=90°				
			Quality of fit		
	Weight	Error	Region 1	Region 2	Region 3
UT-longitudinal	0.1000	0.0063	0.5038	0.5833	0.6004
UT-transverse	0.9000	0.0122	0.4693	0	2.6674
Total	1.0000	0.0985	0.5161	1.0527	3.2678

Table C.7: Identified parameters and error bounds for NY model based on rectus sheath dataset

NY model [51]					
Simultaneous fitting (rectus sheath dataset)					
Parameters	k_0=0.8366 $[MPa]$ k_1=6.3492 k_2=25.7852 φ=90°				
			Quality of fit		
	Weight	Error	Region 1	Region 2	Region 3
UT-longitudinal	0.1015	$2.7021e-04$	0.0252	0.0279	0.0287
UT-transverse	0.8985	$6.8242e-04$	0.0275	0.0557	0.0663
Total	1.0000	$9.5263e-04$	0.0526	0.0836	0.0949

Table C.8: Identified parameters and error bounds for OS model based on rectus sheath dataset

OS model [53]					
Simultaneous fitting (rectus sheath dataset)					
Parameters	μ=0.6971 $[MPa]$ k_1=0.3315 $[MPa]$ J_h=0.1381 J_m=0.3263 φ=90°				
			Quality of fit		
	Weight	Error	Region 1	Region 2	Region 3
UT-longitudinal	0.9000	0.0173	2.2566	2.6379	2.7472
UT-transverse	0.1000	0.0021	0.4551	0.6240	0.6351
Total	1.0000	0.0194	2.7117	3.2618	3.3823

Table C.9: Identified parameters and error bounds for DBB model based on rectus sheath dataset

DBB model [22]					
Simultaneous fitting (rectus sheath dataset)					
Parameters	G=0.1258 $[MPa]$		k_1=3.3666 $[MPa]$		k_2=7.7372
	φ=90°		σ=0.7854		ϕ_{tot}=0.5
			Quality of fit		
	Weight	Error	Region 1	Region 2	Region 3
UT-longitudinal	0.1000	0.0312	1.1734	1.4943	1.7456
UT-transverse	0.9000	0.0223	1.1101	0.1550	0.6958
Total	1.0000	0.0535	1.2835	1.6493	2.4414